Atomic beam preparation for quantum optics experiments

Cornelussen, R.A.

Award date:
1999

Eindhoven University of Technology
Faculty of Applied Physics
Theoretical and Experimental Atomic Physics and Quantum Electronics Group

Atomic Beam preparation for Quantum Optics Experiments

R.A. Cornelussen

VDF/NO 99-02
march 1999

Supervisors:
Ir. A.E.A. Koolen
Dr. K.A.H. van Leeuwen
Prof. dr. H.C.W. Beijerinck

Summary

In order to perform high precision quantum optics experiments, an atomic beam consisting of He^* atoms is prepared. To achieve the objective of a very intense and highly monochromatic beam, laser cooling techniques are applied. First a collimation section, in which transverse Doppler cooling is applied, is used to capture atoms from the source into a parallel beam. Secondly a Zeeman compensated slowing technique is used to decrease the atom's velocity and to obtain a low longitudinal velocity spread. Finally a compression section is added to increase the intensity of the atomic beam. The experimental setup and the effects of the first two laser cooling sections on the properties of the atomic beam are discussed in this thesis.

Two lasers were frequency stabilized. The laser for the collimator was stabilized to approximately the atomic transition frequency of the $2^3S_1 \leftrightarrow 2^3P_2$ transition of helium atoms, using saturated absorption spectroscopy. The laser frequency is stable to within $0.5(2\pi)$ MHz and is known to within $2(2\pi)$ MHz. The laser for the Zeeman slower was stabilized to a detuning of $-740(2\pi)$ MHz from the same transition by periodically measuring the frequency and compensating for any drift. The frequency information was obtained from heterodyne mixing of the stabilized collimator laser and the Zeeman laser.

The collimator captures 1.5×10^{11} He^*s^{-1}, emitted from a source with an intensity of 4×10^{14} $He^*s^{-1}sr^{-1}$, within the residual divergence of (0.7 ± 0.1) mrad of the atomic beam. The residual divergence is defined as the angle between the beam axis and the line through the HWHM of the atomic beam profiles at different positions. These results were obtained using a flat wavefront and about 4 linewidths red detuning of the laser. Using curved wavefronts resulted in a higher residual divergence.

The Zeeman slower slows the atoms to a final velocity of 255 m/s with a velocity spread of 23 m/s FWHM. The transverse velocity spread of the slowed atomic beam is 13.5 m/s FWHM. These parameters were determined using absorption spectroscopy. It could not be determined whether atoms left the Zeeman slower with a too high velocity, due to errors introduced because the derivative of the absorption spectrum is measured. The number of slowed atoms is determined to be approximately 7×10^{10} He^*s^{-1}.

Contents

Chapter 1

Introduction

1.1 Quantum non demolition experiment

In the quantum non demolition (QND) experiment the deflection of an atomic beam by a standing light field in a high finesse optical cavity will be measured. The goal is to show the quantum nature of light by measuring deflection patterns which can only be described with a full quantum mechanical description of the light field in the cavity.

According to quantum mechanics, the light field in the cavity will generally be in a coherent state

$$|\alpha\rangle = e^{-\frac{1}{2}|\alpha|^2} \sum_{n=0}^{\infty} \frac{\alpha^n}{\sqrt{n!}} |n\rangle, \tag{1.1}$$

in which $|n\rangle$ is a photon number state, or a Fock state, with n photons. The Fock states $|n\rangle$, with $n \neq 0$ cause deflection of the atoms, the $|0\rangle$ Fock state (state with no photons present) does not contribute to the deflection.

The experiment is a quantum non demolition experiment because the number of photons in the cavity is preserved. This is because only atoms which have only encountered absorption and stimulated emission processes are considered. The momentum change these atoms encounter when passing the standing light field is an integer multiple of $2\hbar k$, with $\hbar$ Dirac's constant and k the wavenumber of the light used. To understand this, the standing

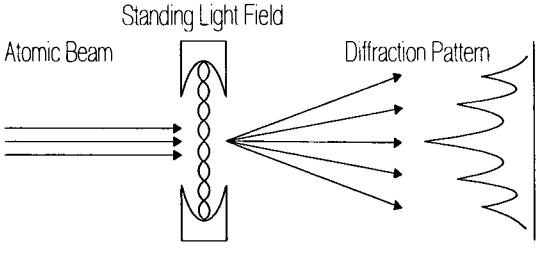

Figure 1.1: Schematic representation of the QND experiment.

light field can be described by two counterpropagating light waves. Every absorption of a photon from one of the light waves must be followed by the stimulated emission of a photon in one of the two light waves. If the latter photon is emitted in the same light wave it was absorbed from, no deflection occurs, but if the photon is emitted in the other light wave a deflection of $2\hbar k$ occurs. This process can be repeated several times.

When the atom has decayed spontaneously, the atom is detected outside the grid with $2\hbar k$ periodicity. This way it is easily distinguished from an atom which has not decayed spontaneously. These events are neglected in order to have a quantum non demolition experiment.

To observe quantum mechanical effects of the light field, the average number $\langle n \rangle = |\alpha|^2$ of photons inside the cavity should be smaller than 1. In this case only the Fock states $|0\rangle$ and $|1\rangle$ are occupied significantly. The population of state $|2\rangle$ is much smaller than the population of state $|1\rangle$ especially. In this low photon limit, the deflection is thus mainly accounted for by the deflection of one Fock state. The experimental conditions can be set such that the deflection from the $|1\rangle$ state is mainly over $4\hbar k$. Almost no deflection over $2\hbar k$ occurs. Many atoms are not deflected. The number of atoms deflected over $4\hbar k$ will be larger than the number of atoms deflected over $2\hbar k$, which is characteristic for a quantum mechanical description of the light field.

Classically, the light field inside the cavity is a standing light field with a certain amplitude of the electric field vector. The deflection still occurs in integer multiples of $2\hbar k$, when no spontaneous emission is considered. This is a consequence of the spatial periodicity of the light field. In the classical case however, the deflection over $4\hbar k$ can not be favored over the deflection over $2\hbar k$. The number of atoms deflected over $2\hbar k$ is larger than the number of atoms deflected over $4\hbar k$.

1.2 Experimental conditions

For the atoms in the atomic beam, metastable helium has been chosen. This is, among other things, because of the possibility to apply laser cooling techniques to these atoms and because single metastable helium atoms can be detected due to their high internal energy. The decay time of the upper level of the atom is within an acceptable range for laser cooling and for the final quantum optics experiment. The main reason for using metastable helium instead of other metastable inert gas atoms is its low mass. Therefore they have a large recoil velocity, which results in relatively large deflection angles in the experiment. Considerations on the detection resolution require a transverse velocity spread of the atomic beam smaller than $0.2\frac{\hbar k}{m} = 18.4$ mm/s. The axial velocity spread should be as small as possible to make sure that the interaction time of all the atoms is the same.

The experiment should be performed in the strong coupling regime. This means that the interaction strength Ω, which is the single photon Rabi frequency, should be larger than the atomic decay time Γ. The relation between the interaction strength and the mirror

distance d of the cavity mirrors is given by

$$\Omega \simeq d^{-3/4}. \tag{1.2}$$

A small mirror distance is needed to have a large interaction strength.

The interaction time τ_i should be not too short in order to make sure that an atom has several interactions with the photon in the cavity. Simulations have shown that to observe a diffraction in which the $|1\rangle$ Fock state mainly deflects in the $4\hbar k$ direction, the interaction time must satisfy

$$\Omega\tau_i \approx 8. \tag{1.3}$$

This is implemented by choosing a certain velocity of the atoms in the atomic beam.

In order to make sure that the atoms interact with an almost constant light field, the decay time of the cavity τ_c has to be larger than the interaction time τ_i. The energy decay time of the cavity is given by

$$\tau_c = \frac{\mathcal{F}d}{\pi c}, \tag{1.4}$$

with $\mathcal{F}$ the reflective finesse $\mathcal{F} = \frac{\pi R}{1-R}$, R the intensity reflectivity coefficient and d the distance between the mirrors. Having the decay time larger than the interaction time τ_i demands a high value for $\mathcal{F}$ for a given mirror distance, so a value for R close to 1.

1.3 Experimental setup

The cavity consists of two high reflectance mirrors with an intensity reflectivity coefficient of 0.999948, 0.93 mm apart. The waist of the light field inside the cavity is 40 μm, which gives an interaction length of about 100 μm. The ringdown finesse of the cavity for the TEM_{00} mode is 6.5×10^5, see [JON98]. This gives an energy decay time of 640 ns. With the optimal velocity of the atoms of 260 m/s the interaction time of an atom with the light field is 400 ns, which is smaller than the energy decay time of the cavity. During the passage of an atom the light field can thus be considered approximately constant. The cavity acts as a Fabry-Perot interferometer with a bandwidth of 250 kHz.

The beam of metastable helium atoms is produced in a liquid nitrogen cooled, supersonic expansion, discharge excited source, described in appendix B. This source has a most probable axial velocity of 1300 m/s [HAB97]. Its center line intensity is about 4×10^{14} He^* s^{-1} $srad^{-1}$, see section 3.3.2.3. The axial velocity of these atoms is too high and the velocity spreads in axial and transverse directions are too large to perform this experiment.

To decrease the axial velocity and the axial velocity spread a Zeeman slowing section is included in the setup. This section will be discussed in chapter 4. By means of light pressure the mean axial velocity is decreased to 260 m/s and the axial velocity spread is

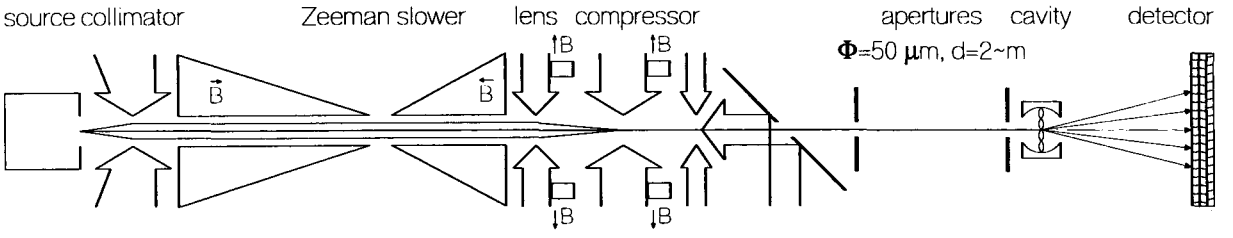

Figure 1.2: Schematic overview of the entire setup.

reduced to less then 15 m/s. A side effect of this slowing process is that both the diameter and the transverse velocity spread of the atomic beam are increased.

To decrease the transverse velocity spread two apertures of 50 μm diameter, which are placed 2 m apart, are placed behind the Zeeman slowing section. These apertures guarantee a transverse velocity spread of maximum 6 mm/s, much lower than the recoil velocity of metastable helium, which is 92 mm/s.

This setup satisfies the demands on the velocity spreads, but estimates of the signal, based on Monte-Carlo simulations [KNO98], have shown that the signal after the two apertures would only be 0.33 mHz. This means that about once every 50 minutes a particle will pass the apertures and reach the detector. This is far below the noise level and thus no analysis can be done. To improve this, some laser-cooling elements are added to the beam setup.

First a collimating section is added, which is discussed in more detail in chapter 3. This section is placed before the Zeeman slowing section and is used to capture atoms from the source into a parallel beam. Therefore, many atoms, which would first have hit the side of the setup, will now reach the end of the Zeeman slowing section. Simulations have shown that including this collimating section increases the beam signal through the apertures with about a factor 4.2.

Secondly a compressing section is added. This section is placed between the Zeeman slowing section and the apertures and is used to make a very intense, parallel beam of small diameter to get as many atoms through the apertures as possible. It actually consists of three parts. First a magneto optical lens (MOL) which focuses the atoms to the axis. It has a focal length of 0.6 m. In this focus the actual magneto optical compressor (MOC) is placed, which compresses all atoms in a beam of small diameter. Finally a transverse Doppler cooling section is added to reduce transverse velocity spreads. Simulations have shown that the resulting beam diameter is 200 μm and that adding these elements increases the beam signal through the cavity with about a factor 5×10^6, which makes the signal detectable. The final signal estimate is 7 kHz.

The signal is detected on a 2D position sensitive detector, positioned 2 m behind the cavity. It consists of a triple MCP array with a resistive anode. It has a resolution of about 100 μm, and thus satisfies the demands on detection resolution. A schematic overview of the entire setup is shown in figure 1.2.

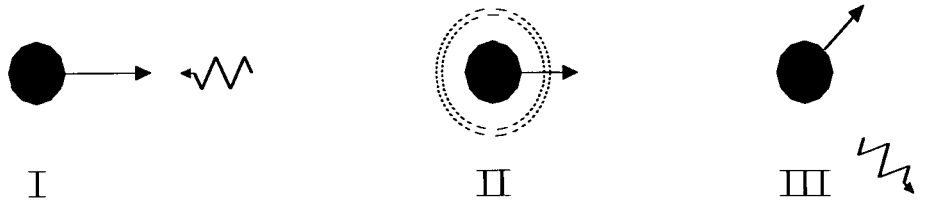

Figure 1.3: Schematic representation of the effect of laser cooling. I: atom can absorb photon, II: photon is absorbed, atom gains its momentum, III: photon is emitted spontaneously.

1.4 Laser - atom interactions

1.4.1 Laser cooling

Consider a two level atom which is initially in the ground state and resonant with the laser. The process described next is schematically shown in figure 1.3. The atom can absorb a photon from the beam of light with momentum $\hbar\vec{k}$ (I) and gain its momentum (II). When the atom decays to the ground state by stimulated emission of a photon the atoms momentum has not changed effectively, but when the atom decays to the ground state by spontaneous emission a net momentum change has occurred (III), because the photon can be emitted in an arbitrary direction.

When an atom undergoes many absorption / spontaneous emission cycles the momentum change due to all spontaneously emitted photons averages to zero and a net momentum change in the direction of the laser beam remains. This momentum change is proportional to the number of spontaneous decays in the time interval considered and the momentum change per absorbed photon $\hbar k$. The force due to the light beam is the first derivative of the momentum and is thus

$$F = \rho_{ee}\Gamma\hbar k, \tag{1.5}$$

in which $\Gamma\rho_{ee}$ is the number of spontaneous decays per second, Γ is the spontaneous emission rate and ρ_{ee} is the occupation number of the upper level.

For the occupation number of the upper level, [BEY93] gives

$$\rho_{ee} = \frac{s}{2(s+1)} = \frac{s_0/2}{1 + s_0 + \left(\frac{2\delta}{\Gamma}\right)^2}. \tag{1.6}$$

In this equation s is the saturation parameter, which is twice the transition rate induced by the light field scaled with the spontaneous transition rate. In this parameter the atomic linewidth is taken into account:

$$s = \frac{|\Omega|^2/2}{\left(\frac{\Gamma}{2}\right)^2 + \delta^2}, \tag{1.7}$$

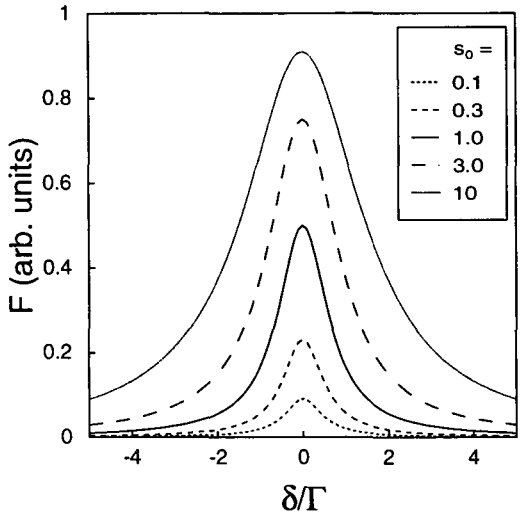

Figure 1.4: The light pressure force as a function of detuning for different values of the saturation parameter.

with Ω the Rabi frequency of the light field, a measure of the electric field strength of the light field, and δ the detuning of the light field from the atomic transition frequency. The saturation parameter on resonance can be written as

$$s_0 = \frac{2|\Omega|^2}{\Gamma^2} = \frac{I}{I_0}, \tag{1.8}$$

with I the intensity of the light and I_0 the saturation intensity of the atomic transition, i.e. the intensity for which a quarter of the atoms is in the excited state.

Using equation (1.6) in equation (1.5) gives

$$F = \frac{\hbar k \Gamma}{2} \frac{s_0}{1 + s_0 + \left(\frac{2\delta}{\Gamma}\right)^2}. \tag{1.9}$$

In this equation δ can be considered an effective detuning, effects of Doppler shifts and Zeeman shifts can be taken into account in this parameter. Figure 1.4 shows the light pressure force as a function of the detuning δ for different values of s_0.

1.4.2 Doppler limit

Although laser cooling works because of the random direction in which a spontaneous emitted photon is emitted, this also limits the cooling. For small velocities the diffusion of the atoms is of the same magnitude as the damping. In [GOR80] an expression for the diffusion of the atoms is given. When the cooling and the diffusion are of the same magnitude, the lower limit of the cooling process is reached, this is called the Doppler limit.

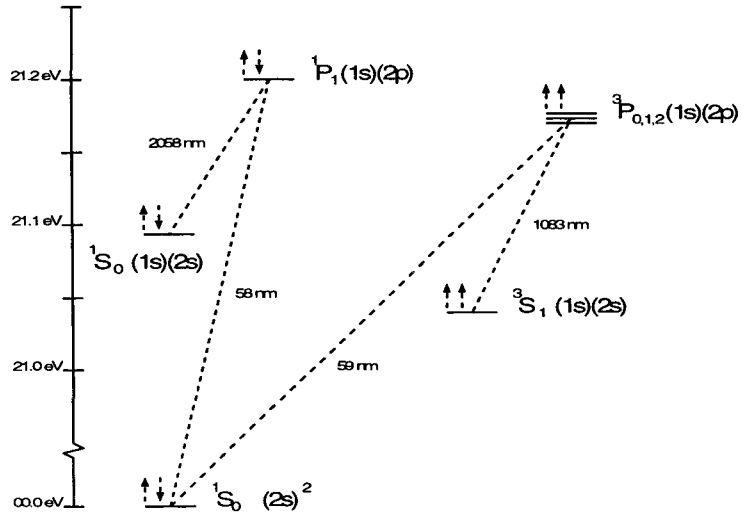

Figure 1.5: Levelscheme of helium. The wavelengths of the transitions are shown.

In terms of velocity, this Doppler limit can be expressed as the minimum achievable velocity spread. For the $2^3S_1|1,\pm1\rangle \leftrightarrow 2^3P_2|2,\pm2\rangle$ transition of metastable helium this Doppler limit is $v_D = 0.28$ m/s. It must be emphasized that this limit is calculated for a one dimensional cooling process with optimal values for the parameters for the detuning and the saturation parameter, $\delta = -\Gamma/2$ and $s_0 = 2$. When using two dimensional laser cooling, this limit cannot be reached.

1.5 Helium

In figure 1.5 the energy levels of helium are shown. For the laser cooling in our experiment the $2^3S_1 \leftrightarrow 2^3P_2$ transition is used, because this is the strongest of the three $2^3S_1 \leftrightarrow 2^3P_x$ transitions. The 2^3S_1 level cannot decay to the ground state by dipole exchange interaction but only by the much weaker quadrupole exchange interaction. It has a lifetime of about 7874 s. Therefore it is called a metastable level.

Each finestructure level is split in $2J + 1$ magnetic substates, each with a specific value of m, the quantum number for the component of the angular momentum along the quantization axis. In figure 1.6 the relative transition probabilities for the transitions are shown.

To be able to apply the laser cooling techniques discussed in the previous section, a two level atom is needed. Metastable helium is not, because normally several transitions are possible, see figure 1.6. When using circular polarized $\sigma^{\pm}$ light metastable helium can be considered a two level atom.

Consider a group of atoms which are in a σ^+ light field. Atoms which are in the $|1,+1\rangle$ state can only make a transition to the $|2,+2\rangle$ state and atoms which are in the $|2,+2\rangle$ state can only, by stimulated and spontaneous emission, decay to the $|1,+1\rangle$ ground state.

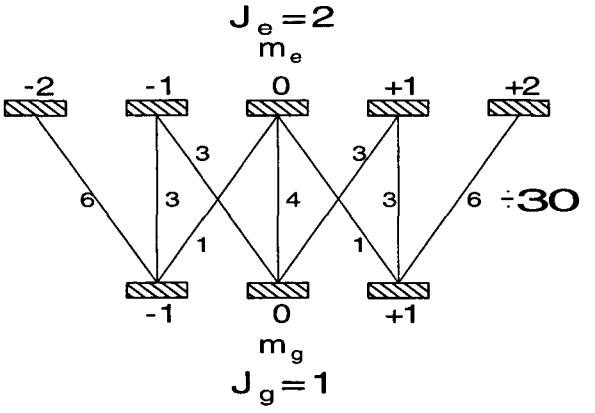

Figure 1.6: Relative transition probabilities.

However atoms which are in another excited state, can decay to various ground states by spontaneously emitting a photon and end up in the $|1,+1\rangle$ state, from which they cannot leave. In the same way atoms which are in a σ^- light field all end up in the $|1,-1\rangle \leftrightarrow |2,-2\rangle$ transition. This process is called optical pumping.

When using $\sigma^\pm$ light, the $2^3S_1|1,\pm1\rangle \leftrightarrow 2^3P_2|2,\pm2\rangle$ transition can effectively be described as a two level atom. From now on the $2^3P_2|2,\pm2\rangle$ level is labeled $|e\rangle$ from excited state end $2^3S_1|1,\pm1\rangle$ is labeled $|g\rangle$ from ground state. Values which concern these two states will be labeled with 'e' end 'g' respectively. For these transitions the saturation intensity $I_0 = 1.67\ \mu\text{W mm}^{-2}$.

It takes several absorption / spontaneous emission cycles before an arbitrary atom is optically pumped. This optical pumping can be destroyed by inelastic collisions or, for a metastable atom, when the atom decays to the ground state.

Transitions for which $m_e = m_g$ are driven by linearly polarized light. Atoms in a linearly polarized light field are, in the steady state situation, distributed over the several ground states with fractions of $\frac{1}{5}$, $\frac{3}{5}$ and $\frac{1}{5}$ for the $m = -1$, $m = 0$ and $m = +1$ substates respectively. This gives a relative transition probability of the transitions for linear light of $\frac{1}{5} \times \frac{3}{30} + \frac{3}{5} \times \frac{4}{30} + \frac{1}{5} \times \frac{3}{30} = \frac{3}{25}$. Transitions for circularly polarized light have a relative transition probability of $\frac{6}{30}$ due to optical pumping. The saturation intensity of linear light is a factor $\frac{6}{30}/\frac{3}{25} = \frac{5}{3}$ times larger then the saturation intensity of circularly polarized light. For linear polarized light the saturation intensity is thus $I_0 = 2.78\ \mu\text{W mm}^{-2}$.

The magnetic substates are degenerate when no external magnetic field is applied. Then metastable helium can also be considered a two level atom when using linearly polarized light. With an external magnetic field applied along the quantization axis the magnetic sublevels are shifted from their bare energies by the Zeeman shift:

$$\Delta E = g \cdot m \cdot \mu_B \cdot B, \tag{1.10}$$

with B the applied magnetic field, μ_B the Bohr magneton $\mu_B = 9.27 \times 10^{-24}$ Am^2 and g

the Landé factor of the level:

$$g = 1 + \frac{J(J+1) + S(S+1) - L(L+1)}{2J(J+1)}. \tag{1.11}$$

For the $^3S_1$ ($L = 0, S = 1, J = 2$) level, $g_g = 2$ and for the $^3P_2$ ($L = 1, S = 1, J = 2$) level, $g_e = \frac{3}{2}$. The angular frequency change of a certain transition when applying a magnetic field is:

$$\Delta\omega = \frac{(g_e m_e - g_g m_g)\mu_B B}{\hbar}. \tag{1.12}$$

The energy differences of all transitions are different. Now using circular polarized light is obligatory to be able to describe metastable helium as a two level atom. In appendix A some characteristic values for metastable helium are given.

Chapter 2

Stabilization of the collimator laser

2.1 Saturated absorption spectroscopy

The laser used for the collimator is, as all lasers used in the experiment, a DBR diodelaser. This type of laser is briefly described in appendix E. For use with the collimator, it must have a frequency close to the atomic absorption frequency of the $2^3S_1 \leftrightarrow 2^3P_2$ transition of metastable helium. It must be actively stabilized to this frequency to compensate for any drift.

To stabilize a laser, information about the frequency of the laser is needed from which an error signal can be created. For stabilizing on an atomic transition the absorption dip in a transmission spectrum seems a good candidate, because the first derivative of this spectrum can directly be used as an error signal: it changes sign at the stabilization point. This error signal can be used to correct the current through the laserdiode. The absorption is typically caused by atoms in a gas cell. A disadvantage is that the width of the absorption dip is about 1.9 GHz, mainly due to Doppler broadening as a consequence of the velocity distribution of the atoms. Various broadening mechanisms in absorption spectroscopy are discussed in [REI98].

This problem can be avoided by using saturated absorption spectroscopy. Using this technique two laser beams of the same frequency propagate in opposite directions through a cloud of metastable helium, as schematically shown in figure 2.1. The two beams should be perfectly spatially overlapping. The first, strong beam ($s > 1$) serves as a pump beam,

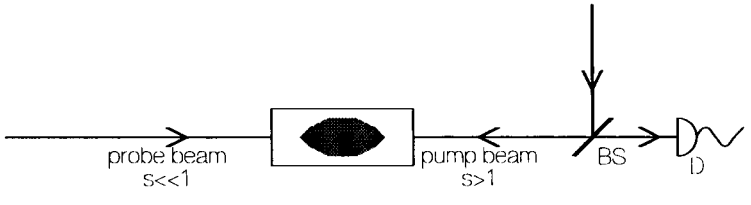

Figure 2.1: Setup for saturated absorption spectroscopy. The strong pump beam saturates the atoms so that the weak probe beam will be less absorbed.

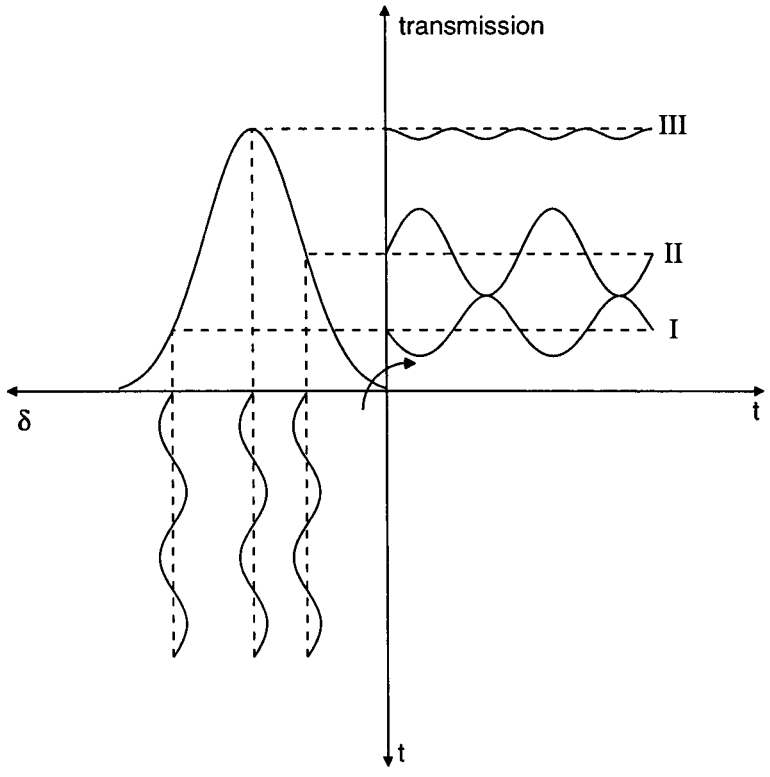

Figure 2.2: Frequency modulation

which saturates the atoms with longitudinal velocities $kv_{pump} = \omega_L - \omega_0$ in which ω_L is the frequency of the laser and ω_0 is the frequency belonging to the desired transition. The second, weak beam ($s \ll 1$) serves as a probe beam and will be resonant with atoms with longitudinal velocities $kv_{probe} = \omega_0 - \omega_L$. Thus, a fraction of the probe beam will be absorbed. If $\omega_L \neq \omega_0$ the probe beam and the pump beam are resonant with different groups of atoms. But if $\omega_L = \omega_0$ the two beams are resonant with the same group of atoms (with zero longitudinal velocity). The probe beam will experience less absorption, because this group of atoms is saturated by the pump beam. A small peak, the saturated absorption peak, will appear in the center of the absorption dip in the transmission spectrum of the probe laser because of this. Its width is free of Doppler broadening and is therefore much smaller than the width of the normal absorption dip. Its first derivative is also a direct measure of the error signal.

2.2 Frequency modulation

A simple way to obtain the first derivative of the saturated absorption spectrum is to modulate the frequency and analyze the transmission spectrum with a phase sensitive amplifier. In figure 2.2 an example is given for varying the reference frequency over a Gaussian peak. In this figure graph I is created by varying the frequency on the left edge

	modulation coil		detuning coil	
number of windings N	100		184	
length l	200	mm	200	mm
diameter d	78	mm	88	mm
resistance R	0.8	Ω	1.4	Ω
$\mathrm{d}B/\mathrm{d}I$	0.59	mT/A	1.06	mT/A
$\mathrm{d}\omega/\mathrm{d}I$, $2^3S_1\|1,1\rangle \leftrightarrow 2^3P_2\|2,2\rangle$ transition	8.18 (2π)	MHz/A	14.80 (2π)	MHz/A

Table 2.1: Some characteristics of the coils used in the saturated absorption setup.

of the saturated absorption peak, graph II by varying the frequency on the right flank and graph III by varying the frequency over the top of the peak. One immediately notices that graph I has the same frequency and the same phase as the input signal, graph II has the same frequency, but its phase is 180° shifted from the input signal and graph III has the double frequency of the input signal. Averaging the product of the transmission signal with the reference signal creates an error signal.

The frequency modulation used in this technique is often obtained by modulating the laser frequency. It is also possible to modulate the atomic absorption frequency and keep the laser frequency constant, because only the difference between the two frequencies is relevant. This can be done by varying the magnetic field along the direction of the light and making use of the Zeeman effect, discussed in paragraph 1.5. This technique has the advantage that there is no modulation on the laser frequency.

2.3 Stabilization setup for the collimator laser

The setup used for stabilizing the laser is schematically shown in figure 2.3. The metastable helium atoms for the absorption are created in a glass cell filled with helium at 0.3 mbar. A small fraction of helium atoms is excited to the metastable $^3S_1$ state by an RF-discharge, which exists over a region of about 1 cm. Concentrically around the cell, two 200 mm long coils are mounted for applying a homogeneous magnetic field in the discharge region. One coil is used to create a modulating magnetic field, and thus to modulate the atomic absorption frequency. The other coil is used to create a constant magnetic field, and thus a constant detuning of the transition. For a coil of length l, diameter d, number of windings N and current through the coil I, the magnetic field in the center of the coil is

$$B = \frac{\mu_0 N I}{\sqrt{d^2 + l^2}}. \tag{2.1}$$

Some characteristics of the two coils are given in table 2.1.

The laser beam for stabilization serves as a pump beam on its first passage through the cell. The probe beam is created by simply returning the pump beam with a mirror. The intensity of this beam is already much smaller than that of the incoming pump beam, because of the large absorption of the pump beam by the metastable atoms. A neutral

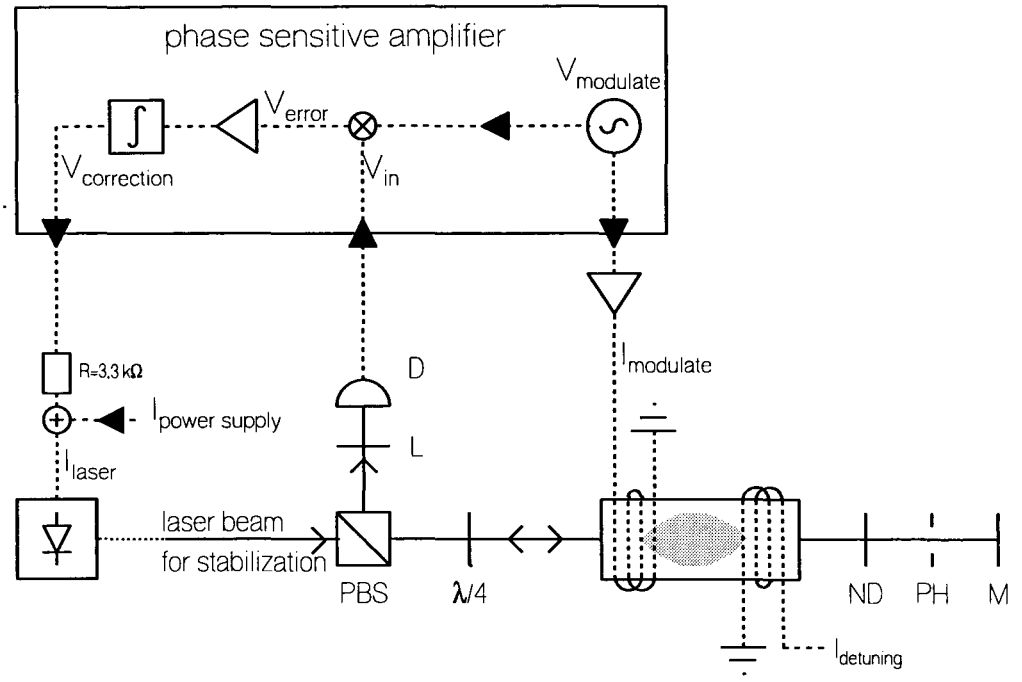

Figure 2.3: Schematic representation of the stabilization setup for the collimator laser. The saturated absorption spectroscopy setup is drawn in solid lines. The electronic feedback to the laser is shown in dotted lines.

density filter may be placed before the mirror to further weaken the probe beam. A pinhole is placed in front of the mirror to make sure that the probe beam is geometrically smaller then the pump beam so that the probe beam only has interaction with a fully saturated set of atoms.

The pump beam first passes a cube beam splitter and a quarter wave plate, which creates circular polarized light for the absorption in the cell. The circular polarized light is necessary to pump the atoms in the gas cell to the strongest transition $2^3S_1(m = 1) \leftrightarrow 2^3P_2(m = 2)$. When this pumping is active the atom can be described as a two level atom. After reflection on the mirror and passing the quarter wave plate, the beam is reflected by the cube beam splitter and it is possible to detect it. The lens is used to focus the beam on the photo detector, which is discussed in appendix F.1.

The magnetic field is modulated with the amplified signal of the internal 1025 Hz oscillator of the phase sensitive amplifier used in the setup. The amplitude of the frequency modulation is about 1 MHz. Finally a constant magnetic field is applied along the direction of the light to stabilize the laser to a slightly different frequency than the atomic absorption frequency. This frequency difference is called the detuning of the laser.

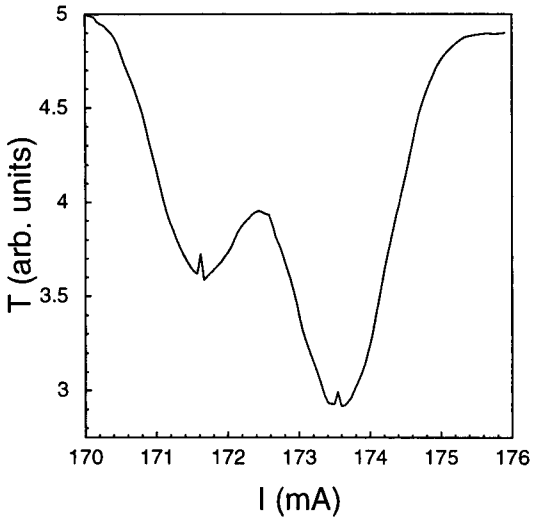

Figure 2.4: The transmission spectrum of the saturated absorption gas cell. The absorption of the ${}^3S_1 \leftrightarrow {}^3P_1$ transition is visible around 171.5 mA and of the ${}^3S_1 \leftrightarrow {}^3P_2$ transition around 173.5 mA.

2.4 Measurements on saturated absorption setup

2.4.1 Dependency of frequency on the laser current

In figure 2.4 a plot of the transmission spectrum of the saturated absorption gas cell, without a magnetic field, is shown. In the spectrum the absorption of the ${}^3S_1 \leftrightarrow {}^3P_1$ and the ${}^3S_1 \leftrightarrow {}^3P_2$ transitions is visible. In the center of these absorption spectra, the saturated absorption peaks are visible.

The frequency difference between the two saturated absorption peaks is well known from literature and is 2291.174(5) MHz, see [SHI94]. The current difference between the two peaks is (1.96 ± 0.02) mA. The frequency dependance on the current through the laser is $(117 \pm 1) \times 10$ MHz/mA.

2.4.2 Accuracy of detuning

In table 2.1 a value for $\mathrm{d}\omega/\mathrm{d}I$ has been calculated for the detuning coil using equation (2.1). Using heterodyne mixing of an unstabilized laser and the collimator laser, stabilized using saturated absorption spectroscopy, the frequency difference of the two lasers for several values of the current through the detuning coil could be determined. In section 4.2.3.2 and appendix H more information about heterodyne mixing is available. With these measurements the value of $\mathrm{d}\omega/\mathrm{d}I = 14.80(2\pi)$ MHz/A given in table 2.1 has been experimentally confirmed, to within 30%.

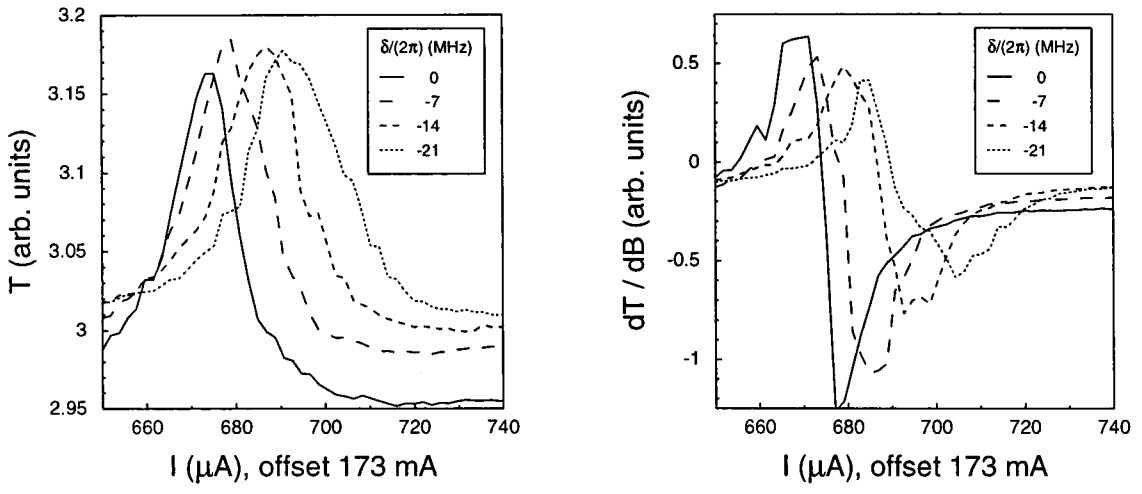

(a) *Transmittance profiles.*

(b) *First derivative of transmittance profiles.*

Figure 2.5: Saturated absorption profiles of the $^3S_1 \leftrightarrow {}^3P_2$ *transition for several detunings.*

In figure 2.5 saturated absorption peaks and their first derivatives, determined using frequency modulation, are shown for various values of the detuning. From these graphs it is clear that the saturated absorption peaks indeed occur at a slightly shifted frequency for the various detunings. The shifts are also clear in the crossings of the zero axis of the first derivatives, which are important because these zero crossings are used to stabilize the laser. The currents for which the first derivatives cross the zero axis are shown in table 2.2. The detunings derived from the values of the currents for these zero crossings do not, within the margin of error, correspond with the set values. This can be caused by a drift of the laser, because only an unstabilized laser could be used to perform these measurements. Also the graphs are not very smooth and consist of only few measured points, to avoid excessive drifts of the laser. The given margin of error does not take these effects into account.

The maximum and minimum of the derivatives are minimally 15 μA apart. This region is the locking region of the setup, where the signal satisfies the demands of an error signal. It is clear from figure 2.5(b) that the measured first derivative has an offset. This offset is caused by the integration circuitry of the phase sensitive amplifier. It results in an asymmetric locking region. Furthermore, this offset shifts the measured zero crossing slightly with respect to the original zero crossing. The resulting offset is about $(1.0 \pm 0.5)(2\pi)$ MHz, but can vary for different settings of the phase sensitive amplifier.

The component of the earth magnetic field along the propagation direction of the light causes a shift. If the total earth's magnetic field, of about 0.5 Gauss, would be along this beam axis, it would give rise to an offset of about $\pm 0.7(2\pi)$ MHz. The sign of this offset depends on whether RHC or LHC polarized laser light is used for the saturated absorption

$\delta/(2\pi)$ (MHz)	laser current at zero crossing (μA, offset 173 mA)	current difference (μA)	laser frequency difference (MHz)
0	674.13 ± 0.07	-	-
-7	678.04 ± 0.07	3.9 ± 0.1	4.6 ± 0.2
-14	686.65 ± 0.07	12.5 ± 0.1	14.6 ± 0.3
-21	689.72 ± 0.08	15.6 ± 0.1	18.2 ± 0.4

Table 2.2: Laser currents for which the first derivative of the saturated absorption peak crosses the zero axis.

spectroscopy. The circularity of the light is not known, so the offset due to the earth's magnetic field is only certainly constant for the same saturated absorption setup.

Although it is possible to vary the detuning of the collimator laser using the saturated absorption setup, it is only possible to compare values of this detuning when the experimental setup has not been changed. Values for the detuning for an unchanged saturated absorption setup can be compared with an accuracy of $0.5(2\pi)$ MHz. Values for the detuning for different saturated absorption setup can be compared with an accuracy of about $2(2\pi)$ MHz, due to the various offsets. Also the absolute values for the detuning are known with an accuracy of $2(2\pi)$ MHz.

2.4.3 Hanle Effect

If the magnetic field in the discharge cell is along the wave vector $\vec{k}$ of the laser beam, the atoms will have interaction with circularly polarized light. Due to, e.g., the earth's magnetic field, the magnetic field vector in the gas discharge cell may not be along the wave vector of the laser beam. The component of the light along the magnetic field, which defines the angular momentum quantization axis of the atoms, consists of a superposition of light with various polarizations. This will counteract the optical pumping.

For strong applied fields, the magnetic field vector is close to the wave vector of the light. The polarization of the laser can be described as circular and the optical pumping is working properly. If the applied magnetic field compensates the longitudinal component of the earth's magnetic field, the magnetic field component perpendicular to the propagation direction of the laser beam can not be neglected. The light with which the atoms are interacting now consists of a superposition of different polarizations. Only a small fraction of the light has the right polarization to be absorbed, so the absorption will decrease.

In a transmission spectrum we observe a small peak in the spectrum, when the applied magnetic field compensates the longitudinal component of the earth's magnetic field.

Chapter 3

Collimator

3.1 Theory of collimator

3.1.1 Doppler cooling

Collimating the atomic beam can be done by using a pair of counter-propagating laser beams with detuning δ, perpendicular to the atomic beam axis. An atom with transverse velocity v now interacts with a laser which is effectively detuned by $\delta - kv$ and with a laser with an effective detuning $\delta + kv$, due to the Doppler shift. The force acting on such an atom follows from equation(1.9):

$$F = \frac{\hbar k \Gamma}{2} \left[\frac{s_0}{1 + s_0 + \left(\frac{2(\delta - kv)}{\Gamma}\right)^2} - \frac{s_0}{1 + s_0 + \left(\frac{2(\delta + kv)}{\Gamma}\right)^2} \right]. \tag{3.1}$$

The velocity dependence of the light pressure force is shown in figure 3.1 for different negative values of δ and $s_0 = 1$. For positive values of δ ('blue detuned light'), the force is repelling; atoms will only be accelerated and are lost. For negative values of δ ('red detuned light), atoms feel a transverse slowing force, with maxima for velocities $v = -v_c$ and $v = v_c$, with $v_c = -\frac{\delta}{k}$, the capture velocity. The main difference in the force for different detunings is the slope of the graph around $v = 0$ and the capture velocity.

The slope of the graph around $v = 0$ determines the amount of cooling of the captured atoms, with the Doppler limit as the lower limit for this cooling. It determines the residual transverse velocity of the atoms. Also the slope of the graph changes for different values of s_0, because the value of s_0 influences the magnitude of the force. To determine optimal values for δ and s_0 for this cooling process, the first order Taylor expansion of equation (3.1) is calculated

$$F \approx \frac{8\hbar k^2 s_0 (\frac{\delta}{\Gamma})}{\left[1 + s_0 + \left(\frac{2\delta}{\Gamma}\right)^2\right]^2} v \equiv -\beta v. \tag{3.2}$$

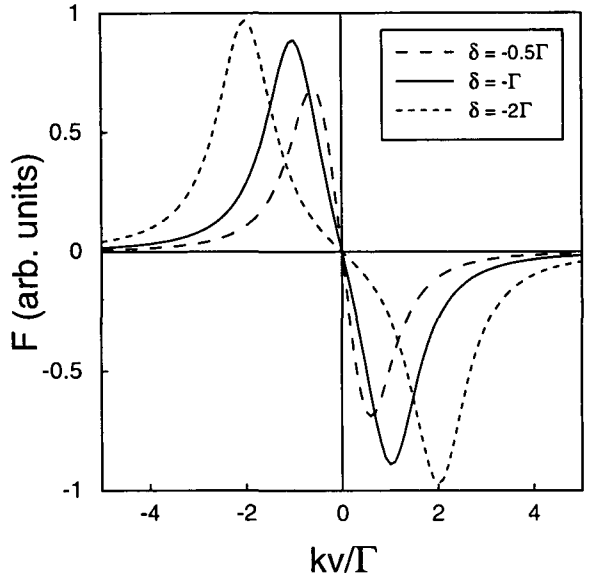

Figure 3.1: The force on an atom due to a pair of counter-propagating laser beams, perpendicular to the atomic beam axis. The graphs are drawn for $s_0 = 1$.

The damping coefficient β has a maximum value for $\delta = -\frac{\Gamma}{2}$ and $s_0 = 2$. The light field is called optical molasses, because for low velocities the slowing force is proportional to the velocity.

For large capture velocities, i.e. large values of $|\delta|$, atoms with large transverse velocities are slowed. In this case, larger values for s_0 result in a larger force and power broadening of the peaks. A larger value of the capture velocity results in a lower damping coefficient β, thereby increasing the final velocity spread.

3.1.2 Curved wavefront technique

A way to capture more atoms is to make use of lasers with curved wavefronts. This is a slightly focused laser with a certain radius of curvature of the wavefront, schematically shown in figure 3.2. The wavefront is parallel to the beam axis at the end of the collimator so that transverse Doppler cooling takes place in this region.

In the beginning of the collimator the light is resonant with atoms moving under an angle θ with respect to the beam axis. The force acting on these atoms is perpendicular to their trajectory, a centripetal force, and they are bended inwards. At the end of the collimator all the captured atoms are Doppler cooled. The capture angle θ_c is defined as half the angle within which the atoms are captured into an atomic beam, moving parallel to the beam axis.

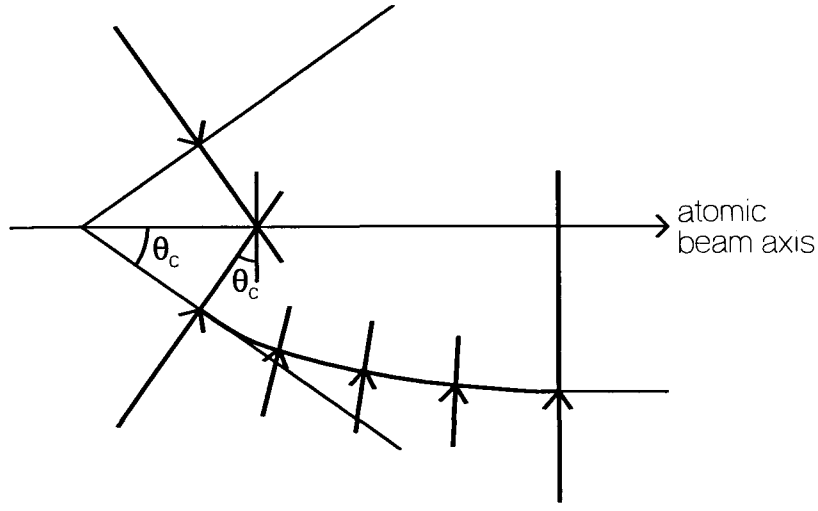

Figure 3.2: The wavefront of the laser is curved. Atoms which move parallel to the local wavefront will be coupled to the wavefront. Atoms that are initially within twice the capture angle θ_c are captured. At the end of the light field there is a region of optical molasses.

3.1.3 Experimental conditions

The atomic beam must be collimated in two dimensions. Therefore two pairs of counter-propagating laser beams, which are orthogonal to each other are used. This effectively decreases the force in one dimension with a factor of two; an atom which is interacting with one pair of laser beams cannot, at the same time, interact with the other pair.

Equation (3.1) was derived using a laser with zero linewidth. The lasers used in the experiment have a linewidth of about 3 MHz, which is about twice the atomic transition linewidth. The actual force is a superposition of the forces induced by the frequency components of the laser. The effective laser power scales with the maximum overlap of the atomic linewidth and the spectral distribution of the laser. For a Gaussian spectral distribution of the light with a FWHM of 3 MHz, the overlap is 0.46. Thus the effective intensity is 46% of the measured intensity of the laser beam. The effective saturation parameter is the saturation parameter calculated using the effective intensity. To avoid heating of the atomic beam it must be taken care of that the entire frequency distribution of the laser is red detuned.

The maximum force acting on a particle with a two dimensional collimator and an effective saturation parameter $s_0 = 2$ is, from equation (1.5), 1×10^{-21} N. Acting as a centripetal force, working on metastable helium atoms with velocity $v = 1300$ ms^{-1}, the capture velocity of the Zeeman slower, this gives a minimum radius of curvature of 11 m. This is equivalent to a capture angle $\theta_c = 15$ mrad in the collimator of length 0.165 m

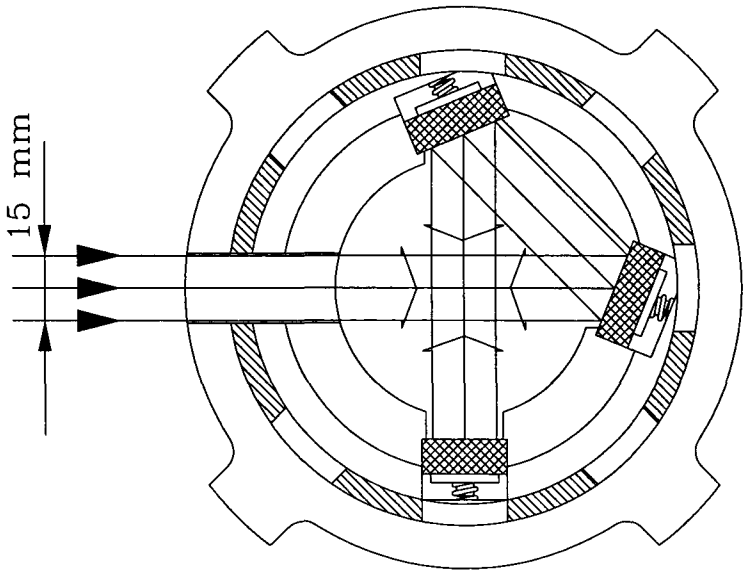

Figure 3.3: Cross-section of the collimator section. The laser beam is recycled by the three mirrors so that the atomic beam is illuminated from four directions using one laser beam.

3.2 Experimental setup

The two counter-propagating laser beams are created using a recycling unit consisting of three gold coated mirrors as shown in figure 3.3. This way the power of the laser beam is recycled and the laser power needed is minimized. A 2% imbalance in the pair of vertical counter-propagating laser beams and of 10% in the pair of horizontal counter propagating laser beams is caused, because the mirrors only reflect 98% of the laser power. The collimator is 165 mm long and is placed directly behind the source in order to capture as many atoms as possible.

A schematic overview of the laser setup is shown in figure 3.4. A DBR diodelaser is used (see appendix E), with an output power of 49 mW. All the optics used is specially coated for 1083 nm. All the mirrors used are gold coated mirrors, with a reflectivity of 98%. The laser is shielded from optical feedback by using an optical isolator (Conoptics, model 715). This isolator attenuates any feedback by 40 dB and linearly polarizes the output beam. Behind the isolator the polarization is made vertical by using a half wave plate (Eksma Quartz, multiple order). This is done to make sure that the polarization of the laser is always in either the p- or the s-plane of reflection for all optical components behind the half wave plate. Some power for stabilization of the laser is split off using a beamsplitter. The beamsplitter consists of a thick glass plate of uncoated BK7 glass (optically flat to $\lambda/10$), so that the two reflections from the frontface and the backface of the glass are spatially separated. About 300 μW is reflected in each beam.

The vertical dimension of the beam is adjusted using an anamorphic prism pair. For this element it is crucial to have the incoming light polarized in the p-plane, so that the

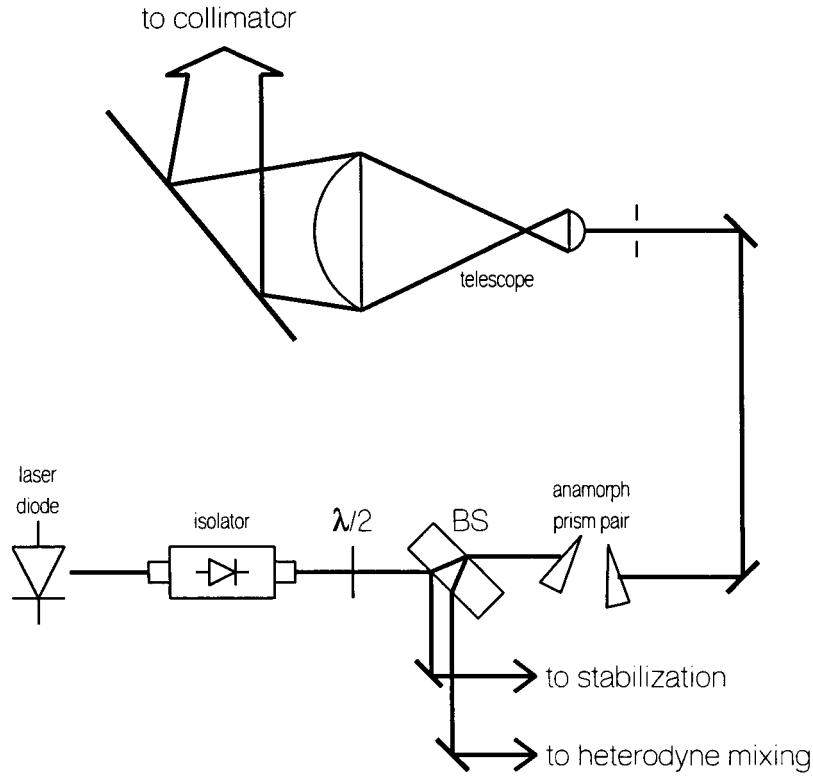

Figure 3.4: Schematic overview of the laser setup

power lost by reflection is very low. The vertical waist is increased to about 3 mm. Behind the anamorphic prism pair, the laser power is 27 mW.

The horizontal dimension of the beam is matched to the size of the collimator, using a telescope consisting of two cylindrical lenses. The first one has a focal distance of 12.7 mm, the second one of 500 mm. This latter lens is an uncoated, plexiglass lens, with a transmittance of 92%. The horizontal waist is increased to 96 mm. The light is then coupled into the collimator using a large mirror and window, which is presumably coated, but has a transmittance of only 93%. The saturation parameter on the beam axis now varies between 18 in the center and 2.5 on the beginning and end of the collimator.

By slightly focussing the beam with the second lens and adjusting the angle of the mirror such that at the end of the collimator the light is orthogonal to the atomic beam axis a curved wavefront is created. The intensity of the laser beam will increase during its passage through the collimator, because the beam is slightly focused. This counteracts the imbalance in the laser power introduced by using a recycling unit as described above.

3.3 Diagnostics on collimator

3.3.1 Beam profile measurements

Information about the atomic beam behind the collimator can be obtained by measuring the beam profile at two places in the beam. From these profiles the number of collimated atoms and the residual divergence of the beam can be determined.

If a metastable atom collides with a conductor an electron is emitted from the conductor. The quantum efficiency of this process approaches unity, because of the high internal energy of the metastable helium atoms (21.03 eV), whereas the energy needed to emit an electron from a conductor is about 5 eV. Charging of the detector is avoided by connecting the conductor to ground. The compensation current from ground is a measure for the number of atoms hitting the detector per unit of time.

The interpretation of the measurements is hampered because several other particles contribute to the measured signal. Electrons from the source reduce the measured signal. High energy UV photons and other metastable helium atoms ($^1S_0$ atoms) increase the signal. The intensity of these particles, and thus their influence on the signal, decreases with the square of the distance from the source, because their trajectories are not affected by laser cooling.

Two kinds of scanners are used. The first is a knife edge scanner which is a sharp edged conducting area that can be moved into the atom beam. The second type of scanner is a wire scanner, a conducting wire that can be moved through the beam. The two types of scanners are extensively discussed in [HAB97].

3.3.2 Measurements with the knife edge scanners

3.3.2.1 Geometry and interpretation of measurements

A knife edge scanner is a conducting rectangular shaped plate, which is larger than the beam size. With this kind of scanner an integrated beam profile is measured. Using two of these scanners directly behind each other, scanning in orthogonal directions gives the possibility to reconstruct the full two dimensional beam profile.

The beam profile was measured with a vertically moving knife edge scanner 125 mm behind the end of the collimator and a horizontally moving knife edge scanner 150 mm behind the end of the collimator. The scanners consists of glass plates of 25×25 mm^2 with the front face of the glass coated with a conducting ITO layer.

It was found that on the vertical scanner a current with the wrong sign could be measured and on the horizontal scanner the current measured was much lower than expected. The reason for these effects is assumed to be electrons from the source hitting the detectors. For the horizontal scanner also emitted electrons returning to the detector contribute to the lower signal. Electrons which are emitted from the detector can be turned by scattering from the background gas or by a magnetic field. The probability of an electron returning to the detector scales with the area of the detector. The vertically moving detector was

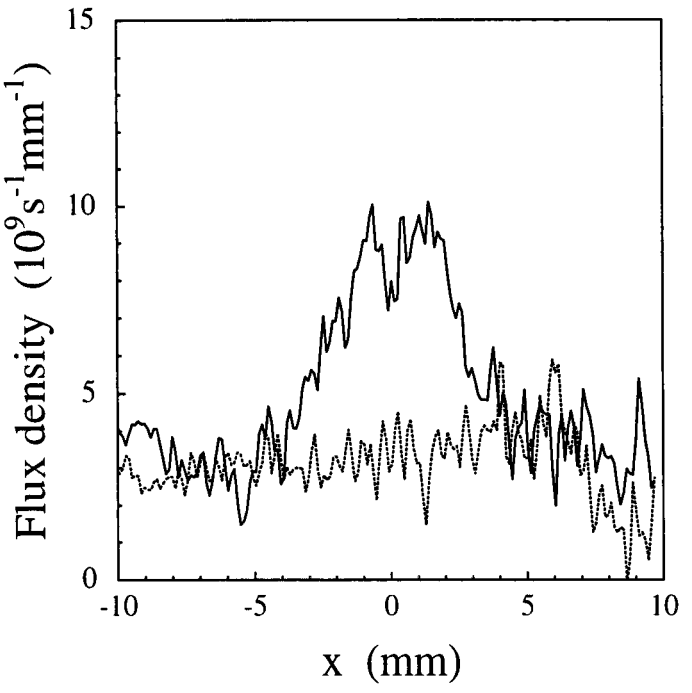

Figure 3.5: Beam profile directly behind the collimator with the collimator on (solid line) and off (dashed line). The profiles are measured with the horizontal knife edge scanner.

now only used to partially shield the horizontal detector. Furthermore a voltage of +500 V was placed on the vertical detector to prevent electrons from returning to the horizontal detector.

Behind the knife edge scanners a 2D detector was placed. It consisted of a metal mesh from which electrons were emitted by colliding metastable atoms. These electrons were accelerated to a phosphor screen by a voltage of 7 kV over 1 cm. The image on the phosphor screen was monitored with a CCD camera. In front of the metal mesh a voltage of 600 V was used to deflect electrons and other charged particles emitted from the source. This 2D detector could not be used to measure the beam profile quantitatively, but was used as a visual aid in tuning the collimator.

3.3.2.2 Measurement of the beam profile

Measurements of the beam profile with the knife edge scanner showed severe problems. The measured signal is the integrated flux density of the beam. The beam profile can be obtained from the measured signal by taking the first derivative of this signal. This causes large spikes in the calculated beam profile for any noise in this measured signal. Only a highly smoothed version of the measured signal can be used to derive a sensible beam profile. Fluctuations in the source intensity created a high noise level which made the interpretation of the measurements very hard.

An example of a beam profile measured with the knife edge scanner is shown in figure

3.5. The capture angle was $\theta_c = 16$ mrad. The contribution of $^3S_1$ metastable atoms, UV photons and electrons to the measured signal is significant, because the scanners are located so close to the source. To compensate for this effect, the difference between the measurements with the collimator on and the collimator off is taken. Both measurements are performed with partial shielding by the vertical scanner to reduce the influence of the non collimated atoms. The profile with collimator off was measured using the same partial shielding as in the measurement with the collimator on.

The knife edge scanners were not used any further, because the processing and interpretation of the data is hardly possible.

3.3.2.3 Center line intensity of the source

The center line intensity of the source can be determined by dividing the flux of atoms in a small region around the center by the solid angle this region occupies. The area around the center is determined in vertical direction by blocking the horizontal scanner at two different positions with the vertical scanner. In horizontal direction the region is defined by measuring at two different positions with the horizontal scanner.

The area was 20.6 mm^2. With the distance between the knife edge scanner and the skimmer of the source of 342 mm, this gives a solid angle of the detection area of 1.76×10^{-4} sr.

The flux of particles in this region is 8.5×10^9 s^{-1}. In [MAS97] is shown, by atomic beam deflection spectroscopy, that 90% of the emitted particles of a Shimizu type metastable helium source are metastable helium atoms in the $^3S_1$ state. It is assumed that this percentage is also valid for the source used in this setup. This gives a center line intensity of the source of 4×10^{14} He*s^{-1}sr^{-1}.

3.3.3 Measurements with the cross wire scanners

3.3.3.1 Geometry and interpretation of measurements

A wire scanner is a conducting rectangular shaped area with one dimension larger than the beam size and one dimension much smaller than the beam size. This way a one dimensional atom density profile can be measured.

A drawing of a cross wire scanner is shown in figure 3.6. It consists of a metal frame in which two wires are connected. The wires are isolated from the frame and from each other. They make an angle of 45° with the direction of movement and are orthogonal to each other. They are not symmetrically connected to the frame. By moving the scanner through the beam, wire scans in two directions are made simultaneously. The displacement of the wires is orthogonal to their direction and is thus a factor $\sqrt{2}$ less than the displacement of the scanner.

With the given geometry the position of the maximum of the atomic beam profile can be determined from the measurements. The horizontal position of the atomic beam follows from the difference in scanner positions for the maxima of both wires. The vertical

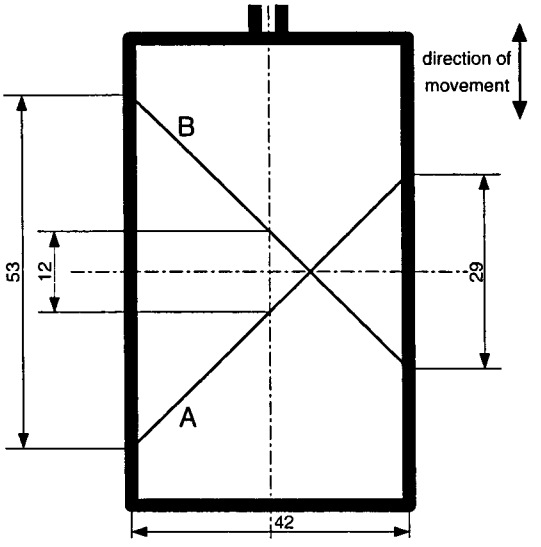

Figure 3.6: Schematic representation of the wire scanner, viewed into the atomic beam. The wires are labeled A and B.

position is determined by comparing the mean value of the positions of these maxima with the known position for which the wires are symmetrically around the beam axis.

There are two cross wire scanners used in the setup. One is placed in the zero magnetic field section of the Zeeman slower, 1.9 m behind the end of the collimator. The other is located in the vacuum chamber for the compressor, 3.85 m behind the collimator. The wires are 0.1 mm thick. The effects of electrons, UV photons and other not lasercooled particles are negligible because the scanners are located so far from the source. This also follows from the measurements. From the measurement of beam profiles at two different positions in the beam, the number of collimated particles and the residual divergence of the atomic beam can be determined.

3.3.3.2 Signal discrepancy between two wires

A problem which is encountered when determining the number of collimated particles is that the signal on wire B is higher than the signal on wire A. The origin of this discrepancy is not fully understood. It may be caused by secondary electrons mainly returning to wire A. This is probably only a small effect because of the small diameter, and therefore a small solid angle, of the wires. Another possibility is that also badly collimated atoms contribute to the signal on wire B and not on wire A. These atoms should be positioned too high and too far to the left of the detector to be measured with wire A. This solution is highly unlikely, because the FWHM of both wires is about equal and thus the calculated residual divergence of the atomic beam is equal in both dimensions. The most likely explanation is that the quantum efficiency of both wires is differently affected by the magnetic fields around the scanners. This is possible due to the different orientation of both wires on a scanner and because the currents that are measured are very small.

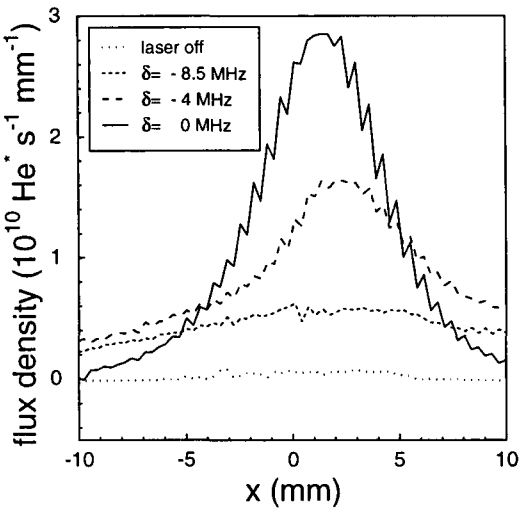

Figure 3.7: Beam profiles for various values of the detuning of the collimator laser at 1.9 m behind the end of the collimator, with a capture angle $\theta_c = 16$ mrad.

The problem only exists when interpreting the data quantitatively. Values for the FWHM of the signal are not influenced by the discrepancy. When trying to interpret the data quantitatively, i.e., determining the number of collimated particles, the flux within the FWHM of the beam profile measured with wire B is used. Although the quantum efficiency of the detector wires may be affected, it will probable not be increased. When a quantum efficiency of 1 is considered, the derived flux densities will still be an upper limit.

The spikes in some of the graphs are caused by an irregularity of the vacuum feedthrough on which the wire scanner is mounted. This causes a transverse movement of the wires-canner.

3.3.3.3 Influence of different detunings of the collimator laser

Using a curved wavefront with approximately the optimal curvature calculated in paragraph 3.1.3, $\theta_c = 16$ mrad, some measurements of the beam profile at 1.9 m behind the end of the collimator were performed. These measurements are shown in figure 3.7. Measurements for values of the detuning of $-8.5(2\pi)$ MHz, $-5.6(2\pi)$ MHz, 0 MHz and a measurement with the laser off are shown. Comparing the measurement with laser off to the other measurements shows that the contribution of uncollimated particles, particles other than metastable helium atoms in the $^3S_1$ state, to the beam profile of a collimated beam at this distance is negligible.

The measurements shown in figure 3.7 are made in one session. Therefore the values of the detunings can be compared to each other with an accuracy of $0.5(2\pi)$ MHz, as mentioned in section 2.4.2. The absolute values are accurate up to about $2(2\pi)$ MHz. The

$\delta/(2\pi)$	FWHM (mm)	flux through FWHM (10^{11} s^{-1})
0 MHz	6.3 ± 0.6	1.47 ± 0.03
-5.6 MHz	8.3 ± 0.6	1.08 ± 0.03
-8.5 MHz	-	-

Table 3.1: Some parameters of the beam profiles shown in figures 3.7.

strong dependance of the functioning of the collimator on the detuning of the collimator is clear from the beam profile measurements shown in figure 3.7. In table 3.1 some parameters of the measured beam profiles are given.

The maximum number of atoms are captured in a collimated beam with minimal FWHM for zero detuning. This detuning probably already corresponds to a red detuned laser, because any laser power in the spectral distribution of the laser which is blue detuned would cause a repelling force and would decrease the performance of the collimator. For larger negative values of δ the FWHM of the peak increases, indicating a decrease in collimation of the atomic beam. Also the number of collimated particles decreases, shown by the decrease in flux through the FWHM. Due to the large detuning of the collimator laser, the damping coefficient β gets very low, resulting in a larger residual transverse velocity.

In the following measurements on the collimator, the detuning is optimized for a wavefront which is parallel in first order at the end of the collimator. Even a plane wavefront may have imperfections due to spherical aberrations in the wavefront, caused by the second lens of the telescope, which is of rather poor quality. Maximum performance of the collimator is achieved by fine tuning the angle of the mirror used for coupling the light into the collimator section. In this way the imperfections in the last and most essential part of the collimator are minimized.

3.3.3.4 Residual divergence

By measuring a beam profile at two different positions, information about the residual divergence can be obtained. The residual divergence is defined as the angle between the beam axis and the line through the FWHM at different positions. In the setup this can be measured by using the two cross wire scanners 1.9 m and 3.85 m behind the collimator. The latter scanner is behind a circular aperture with a radius of 15 mm. In appendix D it is shown that this aperture hardly affects the measurement when the aperture radius is smaller than the FWHM of the signal, a criterion satisfied by the measurements. Both the measured FWHM and the measured flux are hardly influenced.

Measurements of the beam profile with these two scanners for a capture angle of 16 mrad and $\delta = -4.5(2\pi)$ MHz are shown in figure 3.8(a). The FWHM of these measurements are given in table 3.2. From these measurements the residual divergence, defined as the angle between the atomic beam axis and the line through the HWHM of the beam profiles at different positions, is calculated. An estimate of the transverse velocity spread is made, assuming an axial velocity of 1300 m/s. This transverse velocity spread is about 3.9 m/s FWHM. This velocity spread is about 12 times higher than the Doppler limit for metastable

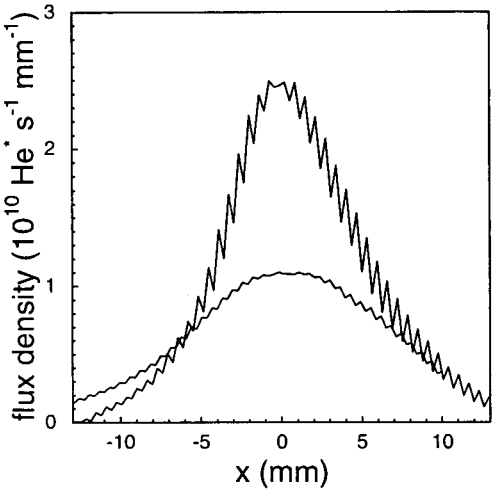

(a) $\theta_c = 16$ *mrad*, $\delta/(2\pi) = -4.5$ *MHz*.

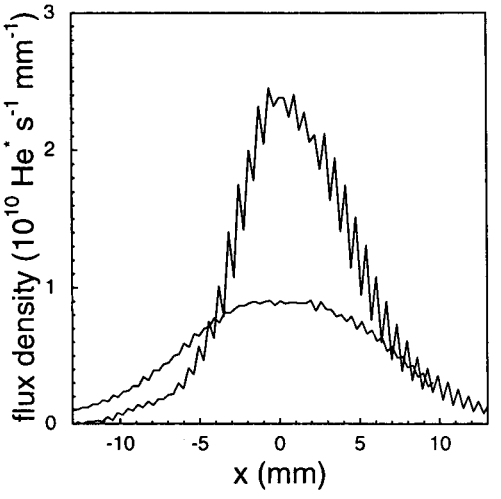

(b) $\theta_c = 12$ *mrad*, $\delta/(2\pi) = -4.5$ *MHz*.

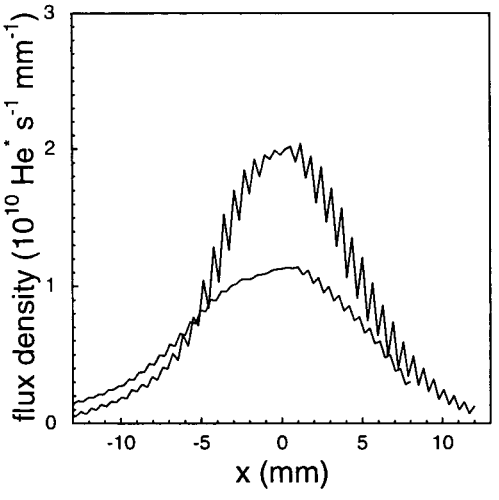

(c) *Plane wavefront*, $\delta/(2\pi) = -7$ *MHz*.

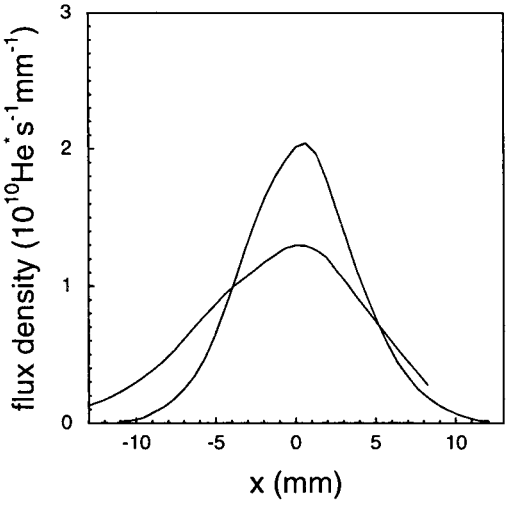

(d) *Plane wavefront*, $\delta/(2\pi) = -4.2$ *MHz*, *shielding of magnetic field.*

Figure 3.8: Beam profiles with various settings of the collimator. The narrow beam profile is at 1.9 m behind the source, the wider profile is measured at 3.85 m behind the source.

nominal capture angle (mrad)	FWHM 1.9 m (mm)	FWHM 3.85 m (mm)	residual divergence (mrad)	transverse velocity spread (m/s)
16	9.2 ± 0.3	15.0 ± 0.3	1.5 ± 0.1	3.9 ± 0.1
12	8.0 ± 0.3	15.0 ± 0.3	1.8 ± 0.1	5.0 ± 0.1
0	9.9 ± 0.3	12.7 ± 0.3	0.7 ± 0.1	1.8 ± 0.1
0, shielding	8.3 ± 0.7	12.1 ± 0.6	1.0 ± 0.3	2.6 ± 0.3

Table 3.2: Calculation of residual divergence for several capture angles of the collimator. The transverse velocity spread is calculated assuming an axial velocity of 1300 m/s.

helium, but this value is derived for one dimensional laser cooling and thus can not be reached in this experiment.

Decreasing the residual divergence may be done by decreasing the capture angle. Atoms having a transverse velocity slightly higher than the capture velocity of the optical molasses will be laser cooled, but may not reach the minimum value for the transverse velocity. These atoms cause a broadening of the measured beam profiles and therefore an increase of the residual divergence. Also faster atoms emitted by the source may not reach the minimum transverse velocity, because their interaction time with the collimator laser is too short. Both effects can be decreased by choosing a smaller capture angle.

To investigate this effect the capture angle has been decreased to 12 mrad, but no drastic changes occurred. The measurements were performed with a detuning of the collimator laser of $\delta/(2\pi) = -4.5$ MHz. The beam profiles for this capture angle are shown in figure 3.8(b); characteristics of these profiles are given in table 3.2. The residual divergence and the transverse velocity spread are even somewhat larger than for the atomic beam collimated with a laser with a capture angle of 16 mrad. Aligning the collimator laser with a plane wavefront and $\delta/(2\pi) = -7$ MHz, decreases the residual divergence and the transverse velocity spread by 50%. The beam profiles are shown in figure 3.8(c) and characteristics are again given in table 3.2.

A reduction of the residual divergence may also be accomplished by reducing the stray magnetic fields of a penning ionization pressure gauge mounted onto the collimator chamber. The magnetic field of this pressure gauge could influence the measurements by introducing a varying Zeeman shift. The residual magnetic fields of this gauge have been shielded using a plate of μ-metal. A measurement of the beam profile with a plate of μ-metal shielding the magnetic field is shown in figure 3.8(d). The beam profile is measured with a plane wavefront and $\delta/(2\pi) = -4.2$ MHz. No improvement is measured with this shielding, it has thus not been used again.

Collisions between collimated particles could cause broadening of the atomic beam. The effect of these collisions is calculated to be negligible (appendix C). Collisions between atoms from the background gas and atoms in the atomic beam are not negligible, but mainly result in loss of particles, due to the large recoil angles.

nominal capture angle (mrad)	flux through FWHM at 1.9 m (10^{11} s^{-1})	flux through FWHM at 3.85 m (10^{11} s^{-1})	measured capture angle (mrad)	flux 3.85 m / flux 1.9 m (%)
16	1.80 ± 0.03	1.34 ± 0.02	12 ± 3	75
12	1.54 ± 0.04	1.12 ± 0.01	11 ± 3	73
0	1.59 ± 0.03	1.18 ± 0.02	11 ± 3	74

Table 3.3: Relation between the flux within the FWHM measured with the two cross wire scanners. The measured capture angle was determined by comparing the flux through the FWHM at 1.9 m with the source intensity measured in paragraph 3.3.2.3.

3.3.3.5 Flux in the collimated beam

Although the measurement with the wire scanners may not be fully interpreted quantitatively, as discussed in section 3.3.3.2, an attempt is made in this section. The measurements of the wires with the highest signals, wires B, are compared to each other, so that measurements of the beam profiles which are closest to the actual beam profiles are compared.

In table 3.3 values for the flux within the FWHM for the measurements of the two wire scanners, shown in figure 3.8 and discussed in section 3.3.3.4, are shown. The decrease in flux in the measurement at 1.9 m behind the collimator and at 3.85 m behind the collimator is obvious for all measurements.

The values of the second wire scanners may be influenced by shielding of this scanner by the aperture with a radius of 15 mm in front of the scanner. In appendix D is shown that this can account for a 4% decrease in flux.

A second cause for a decrease in signal on the second wire scanner may be the destruction or the deflection of metastable atoms by collisions with the background gas. In appendix C an estimate for the transmittance of the background gas is derived for the actual experimental conditions. This transmittance was estimated to be about 83%. Both effects together account for 20% decrease in signal, explaining the flux discrepancy.

The measured flux for the different capture angles can not be compared, because the source intensity may be different. Still it seems that the number of captured particles does not increase significantly for an increasing capture angle. This especially applies to the measurement with the plane wavefront. This is probably caused by the relatively large linewidth of the laser used, which is about 3 MHz or twice the linewidth of the transition, and the large detuning of the collimator laser. Therefore also some power of the spectral distribution of the laser is resonant with atoms with high transverse velocities.

To estimate the influence of the linewidth, experimental values for the measured capture angles, given in table 3.3, are calculated by comparing the measured flux within the FWHM at the first wire scanner with the source intensity of 4×10^{14} $He^{*}s^{-1}sr^{-1}$. The errors are mainly caused by the error in the source intensity, which may be 50%. For the measurement with the plane wavefront this capture angle means that for atoms with an average velocity of 1300 m/s, atoms with transverse velocities up to 14 m/s are captured in a collimated beam. Atoms with a transverse velocity of 14 m/s are resonant with laser light with a

detuning of $13(2\pi)$ MHz. Due to the large detuning of the collimator laser of $7(2\pi)$ MHz and the linewidth of the laser of 3 MHz, this value is plausible.

3.4 Compensation of Zeeman slower's magnetic field

The residual magnetic field of the Zeeman slower magnet can influence the collimator. In the collimation section, on the beam axis, the axial magnetic field has values between 4 Gauss and 16 Gauss for a typical current through the Zeeman slower coil of 3 A, see figure 3.9.

For horizontally polarized light this gives rise to a Zeeman shift. The variation in the Zeeman shift in the beginning and the end of the collimator is too large to have atoms resonant with the laser in the entire collimator section. For vertically polarized light the variation in Zeeman shifts may be smaller, because they are caused by the transverse magnetic field.

A comparison between a measurement of the beam profile for the magnetic field of the Zeeman slower turned off and on is shown in figure 3.10(a). All measurements are performed with a capture angle $\theta_c = 12$ mrad. To reduce the effect of the magnetic field on the performance of the collimator, a coil was added to the set up which compensates for the magnetic field in the collimator section. With this coil, mounted on a connection flange between the collimation section and the Zeeman slowing section, the axial magnetic field can be decreased to values between -0.6 Gauss and 0.4 Gauss.

The distance between the end of the compensation coil and the beginning of the Zeeman slower coil is 45 mm. It is designed to operate at the same current as the Zeeman slower magnet, so that any possible changes in the current through the Zeeman coil are automatically compensated. It has a width of 9.5 mm, an inner radius of 0.12 m and is 14 mm thick. These parameters were calculated by comparing the magnetic field of a winding of this size and the correct current density with the magnetic field simulations of the Zeeman slowing coil. For a current through the Zeeman slower coil of 3 A, the axial magnetic field is canceled to less than 1 Gauss, see figure 3.9.

A measurement of the beam profile with both the magnetic fields of the Zeeman slower and the compensation coil on, is shown in figure 3.10(b). Comparing this measurement with the measurement for the magnetic field of the Zeeman slower turned off, figure 3.10(a), shows that the collimator can be operated when the magnetic field of the Zeeman slower is compensated with an extra compensation magnet.

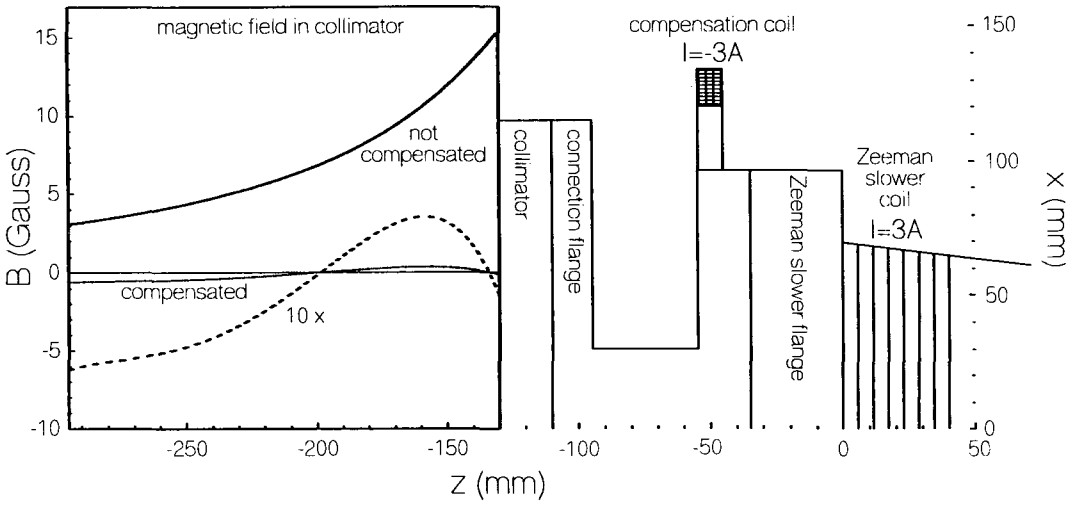

Figure 3.9: The residual axial magnetic field of the Zeeman slowing section in the collimator (solid line) and the magnetic field in the collimator with the compensation coil on (dotted line, 10× amplified). On the right a part of the setup is drawn, with the graph at the place of the collimator. The compensation coil is shown.

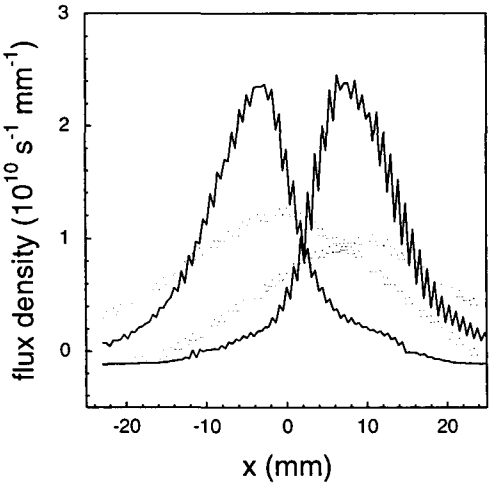

(a) *Comparison for magnetic field of Zeeman slower off (-) and on (△).*

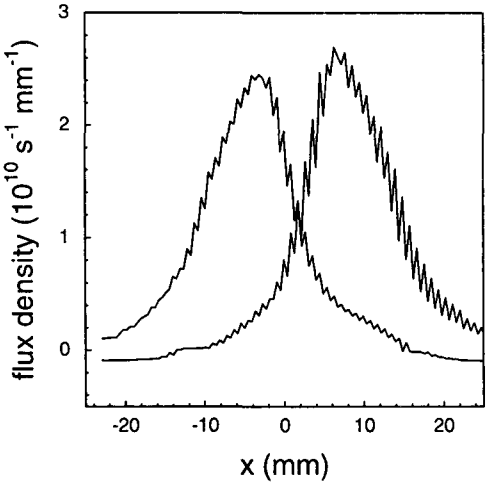

(b) *Magnetic field of Zeeman slower compensated.*

Figure 3.10: Measurements of the atomic beam profile, 1.9 m behind the collimator, to show the effect of the compensation coil.

3.5 Conclusions

Using knife edge scanners for measuring a beam profile is not working in practice. Any noise on the measured signal makes the beam profile, which is the derivative of the measured signal, not interpretable. Smoothing of the measured signal facilitates the interpretation of the beam profiles. Wire scanners, and especially the cross wire scanners used, are a good diagnostics tool for beams of metastable atoms. By using two cross wire scanners at two distances from the collimator, a value for the residual detuning of the atomic beam could be determined. Also an estimate of the flux of captured and collimated atoms could be determined.

The collimator captures about 1.5×10^{11} He^*s^{-1} in a collimated beam with a residual divergence of (0.7 ± 0.1) mrad. This number is achieved using a plane wavefront and a large detuning of the collimator laser of about $-7(2\pi)$ MHz. Using curved wavefronts hardly increased the flux of atoms, while the residual divergence increased rapidly. The reason for this is assumed to be the poor quality of the wavefront of the collimator laser, probably caused by a machined, uncoated plexiglass lens, used to increase the beam size, and the linewidth of the laser.

Due to a high value of the linewidth of the collimator laser and due to a very well performance of the source, which has an intensity of 4×10^{14} $He^*s^{-1}sr^{-1}$, the number of collimated particles is still reasonable.

The collimator will be operated with a plane wavefront and a large detuning of the collimator laser, about $-7(2\pi)$ MHz, four natural linewidths of the transition or two laser linewidths. The reason for this decision is the very good collimation of the beam whereas the number of collimated atoms does not decrease dramatically. It is expected that this better collimation will increase the number of slowed atoms at the end of the Zeeman slower.

Chapter 4

Zeeman slower

4.1 Theory of Zeeman slower

The Zeeman slower is used to decrease both the longitudinal velocity and the velocity spread of the atoms in the atomic beam. This is done by using the light pressure force, as described in paragraph 1.4.1. This causes a slowing force, when the atom is resonant with the laser.

When a particle is slowed down uniformly, its velocity v depends on its position z according to

$$v(z) = v(0)\sqrt{1 - \frac{z}{z_s}} \tag{4.1}$$

as has been derived in appendix G, with $v(0)$ the atom's initial velocity and z_s the stopping length, the distance over which the velocity of the atoms reaches zero if the slowing process would be continued. The distance needed to decrease a particle's speed with a certain factor increases for larger initial velocities.

When the atom decelerates, the Doppler shift changes and the atom loses resonance with the laser. To compensate for this effect, a varying axial magnetic field is applied. The Zeeman shift introduced at a certain place in the Zeeman slower by this magnetic field compensates for the Doppler shift of atoms with a certain velocity. The resonance condition for an atom with axial velocity $v(z)$ now is

$$kv(z) = -\delta + \frac{\mu_B}{\hbar}B(z), \tag{4.2}$$

in which μ_B is the Bohmagneton, $\hbar$ is Dirac's constant, k is the wavenumber of the light used and δ is the detuning of the Zeeman laser.

A uniform deceleration is induced by compensating the Doppler shift of the atoms with a magnetic field with a position dependence like

$$B(z) = B_0 + B_c\sqrt{1 - \frac{z}{z_s}}. \tag{4.3}$$

In this equation $B_0 + B_c$ is the maximum magnetic field at the beginning of the Zeeman slower. With a certain detuning of the laser this determines the maximum velocity with which atoms can be resonant with the laser. In the beginning of the Zeeman slower the gradient of the magnetic field is minimal, because the fastest atoms are decelerated there. By adding a constant magnetic field B_0, it is possible to choose the magnetic field in the end of the Zeeman slower and thereby setting the final velocity of the slowed atoms.

The magnetic field used in the setup is shown in figure 4.1. Consider an atom entering the Zeeman slower with a velocity v_A of 1100 m/s. It has no interaction with the laser until it reaches the position z_A, where the magnetic field and the atom's velocity satisfy the resonance condition, equation (4.2). From there on the atom remains resonant with the laser, because the effects of the varying magnetic field and the decreasing velocity cancel each other. The atom is decelerated to the final velocity from there on. An atom with a larger velocity v_B satisfies the resonance condition at a place closer to the entrance of the Zeeman slower z_B, an atom with a smaller velocity v_C becomes resonant further in the Zeeman slower. Both are decelerated to the same final velocity from there on.

The maximum force on a particle is given by equation (1.9), by substituting a high value for s_0. The deceleration needed to keep resonant with the laser, which is induced by the gradient of the Zeeman slower magnet, must be smaller than the deceleration following from this maximum force. The larger the deceleration needed, the more atoms will lose resonance in the slowing process. This is because the slowing process is based on spontaneous emission of photons, which is a statistical process. An atom can be excited longer than the decay time, which is only an average value, and thereby reducing the effective force that is applied.

An end point of the slowing process is defined by changing the gradient of the magnetic field in sign. Doing this, atoms with higher velocities become resonant with the laser again. The slowed particles can not be decelerated any further. The change in gradient should be as fast as possible, so that the minimum in magnetic field is very sharp defined. The residual velocity spread of the atoms is lower for this last method.

4.2 Experimental realization

4.2.1 Magnetic setup

The atoms should be decelerated from 1300 m/s down to 260 m/s in the Zeeman slower. It is chosen to decelerate the atoms with 66% of the maximum force that can be applied, 3.13×10^{-21} N as given by equation (1.9), thus at 2.07×10^{-21} N. Using equation (G.1) it can be calculated that a slowing region of 2.6 m is needed. This is implemented using a midfield zero configuration consisting of two coils.

The first coil is 1.6 m long, used for slowing atoms with velocities from 800 m/s to 1300 m/s down to a velocity of 800 m/s. It is operated with a current of 3.0 A, creating a magnetic field varying from 318 Gauss in the beginning of the Zeeman slower to 0 Gauss at the end of the first coil. The second coil is 1.0 m long, used for slowing down the atoms

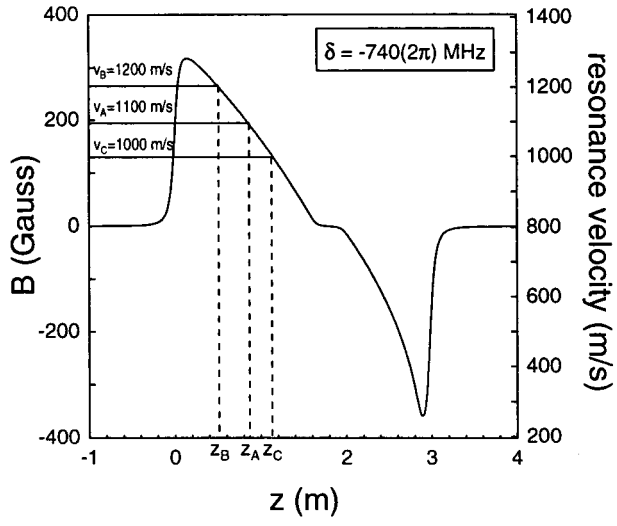

Figure 4.1: The axial magnetic field on the axis of the Zeeman slower when operated at optimal parameters. The current through the first coil is 3 A; the second coil is -2.35 A.

from 800 m/s down to 260 m/s. It is operated with a current of -2.35 A, creating a magnetic field varying from 0 Gauss in the beginning of the second coil to -359 Gauss in the end of the Zeeman slower. The laser must be resonant with atoms at a velocity of 800 m/s and should thus be detuned by $-740(2\pi)$ MHz.

The magnetic field is shown in figure 4.1. The end of the slowing process is defined by a change of the gradient of the magnetic field. Note that in the actual setup the zero magnetic field region in the middle is about 0.5 m longer to be able to place a vacuum pump. This is also the position where the first wire scanner is located. The maximum magnetic field in the beginning of the Zeeman slower is decreased to 313 Gauss, due to the coil used to compensate the residual magnetic field of the Zeeman slower in the collimator section.

4.2.2 Loss of particles and final velocity spread

Due to the random behaviour of the spontaneous emission, which is the basis of the slowing force, the transverse velocity spread increases. It is simulated to be 17 m/s FWHM at the end of the Zeeman slower, see [KNO98]. The atom performs a random walk and both the transverse velocity spread and the diameter of the atomic beam increase during the slowing process. When an atom's distance from the axis gets too large, it can leave the slowing region, due to the finite dimensions of the slowing laser. Simulations have shown that the final diameter of the atomic beam will be 45 mm FWHM, whereas the diameter of the slowing laser is only 30 mm, due to an aperture in the setup. Atoms leaving the light region will leave the Zeeman slower with a velocity higher than the desired final velocity. This

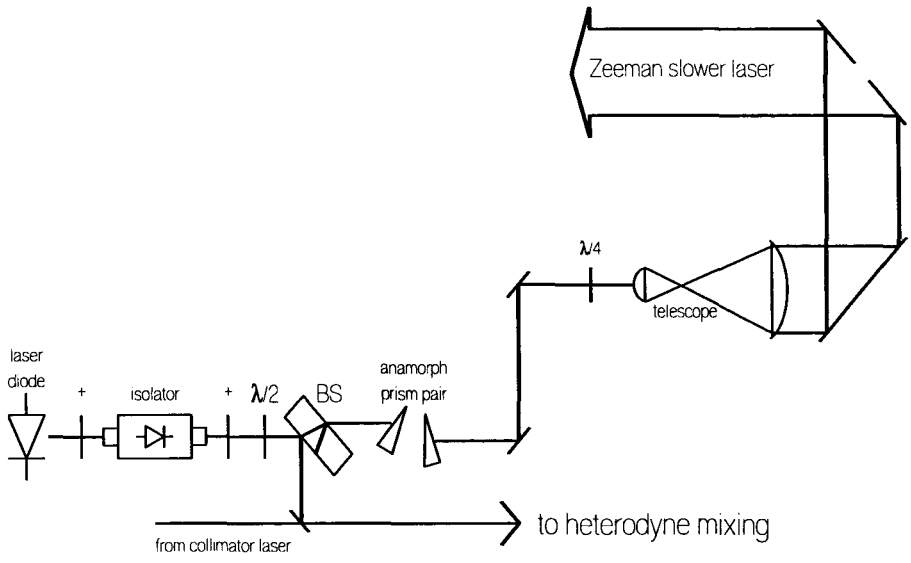

Figure 4.2: Schematic overview of the laser setup for the Zeeman slower.

process mainly occurs at the end of the Zeeman slower, where the diameter of the atomic beam gets larger than the diameter of the slowing laser. This gives rise to broadening of the final velocity distribution.

Due to all optical components in the laser beam, the wavefront of the laser is not perfectly smooth, causing dark regions in the wavefront. When an atom enters such a dark region, it is not slowed down for a while. When it then enters the light region again, the atom is not resonant with the slowing laser anymore. An atom can also lose resonance with the laser due to the discrete steps of the magnetic field due the windings of the coils. The deceleration needed to keep resonant with the laser over such a step may be too large.

The final velocity depends on the magnetic field at the end of the Zeeman slower and the detuning of the laser light, as discussed in section 4.1. The spectral width of the laser increases the velocity spread, because the detuning δ in the resonance condition, equation (4.2) now has a certain spread. For a laser linewidth of 3 MHz the broadening of the velocity distribution is 3.2 m/s.

4.2.3 Laser setup

4.2.3.1 Slowing laser preparation

The laser setup is shown in figure 4.2. The laser used is again a DBR laser, discussed in appendix E. Its output power is 31 mW. The laser beam first passes an optical isolator (OFR, type IO-D-1083) which attenuates any feedback by 46 dB. Two lenses with focal distances of 100 mm and 75 mm are used to focus the laser beam through the isolator, decreasing the beam size with a factor 0.75.

Behind the optical isolator a half wave plate (Eksma, quartz, multiple order) is inserted

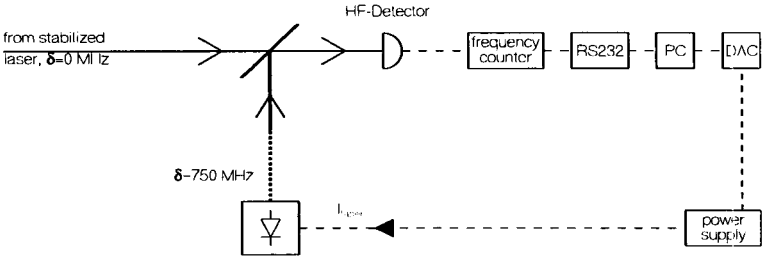

Figure 4.3: Stabilization scheme of the Zeeman slower laser. The optical paths are solid lines, the electronic paths are dotted lines.

to produce vertically polarized light. Some power for stabilization is split of using a beam-splitter. This consists of a thick glass plate (BK7, optically flat over $\lambda/10$), so that the two reflections from the frontface and the backface of the glass are spatially separated. About 200 μW is reflected in each beam. An anamorphic prism pair is used to create a circular beam shape. Behind the prism pair a quarter wave plate is used to create circularly polarized light. The power of the laser behind the quarter wave plate is about 21 mW.

Now two lenses of focal distances $f = 25$ mm and $f = 350$ mm are used to increase the beam size to the desired value. The vertical and the horizontal waists are both 24 mm. The beam has a convergence of about 3 mrad to match the divergence of the atomic beam. The saturation parameter now varies from $s = 9$ in the center to $s = 5.5$ at a radius of 12 mm. With two mirrors the laser beam is directed into the Zeeman slower, as shown in figure 4.2. The quarter wave plate is adjusted such that the polarization is circular in the Zeeman slower beam. Circular light is used to drive the $2^3S_1|1,1\rangle \leftrightarrow 2^3P_2|2,2\rangle$ transition, which is the strongest transition.

4.2.3.2 Stabilization of the Zeeman laser

It is not possible to stabilize this laser using saturated absorption spectroscopy, due to the detuning of $-740(2\pi)$ MHz required for the Zeeman slower laser. The magnetic field to be applied in the gas cell would be too large to keep the discharge running.

The stabilization setup used is shown in figure 4.3. The frequency of the laser can be determined using heterodyne mixing: if some power of the laser for the Zeeman slower and some power of the stabilized laser for the collimator, which is stabilized at a frequency close to resonance, spatially overlap on a photo detector, a beat signal arises. The frequency of this signal is equal to the frequency difference of the two lasers, as derived in appendix H.

The detector used for this measurement is a photodiode with a 5 V bias voltage to increase its bandwidth, see appendix F.2. The signal from this detector is amplified with a pulse preamplifier (Phillips Scientific, model 6954) with a maximum voltage gain of 100 for frequencies between 100 kHz and 1.7 GHz. The frequency is measured with a frequency counter (Voltcraft 7023). The frequency counter is connected to a computer via a RS-232 interface. The frequency of the Zeeman laser is kept constant by periodically measuring the frequency and compensating for any drift. The laser is stabilized within 5 MHz.

4.2.3.3 Effects of aperture in Zeeman mirror

The mirror inside the vacuum system has an aperture in the middle, through which the atoms can pass when the lens and the compressor are working. This aperture causes a shadow in the intensity profile of the laser. The intensity in this shadow region will increase due to diffraction. The matching of the divergence of the Zeeman laser to the divergence of the atomic beam will also increase this intensity.

The intensity of the laser beam after reflection is given by

$$I(z,r) = \left(E_0 e^{-2r^2/w^2} - \frac{2E_0}{z} \frac{J_1\left(kRr/\sqrt{r^2+z^2}\right)}{kRr/\sqrt{r^2+z^2}} \right)^2 . \tag{4.4}$$

The first part describes the Gaussian profile of the laser beam with waist w and maximum amplitude of the electric field vector E_0. The second part describes the diffraction due to an aperture with radius R. The diffraction is described as Fraunhofer diffraction, see e.g. [PED93]. The radius is smaller than the waist of the laser, so that the diffraction can be described as the diffraction of a plane wave with amplitude E_0. J_1 is the first order Bessel fuction of the first kind, k is the wavenumber of the light used.

The intensity on the beam axis does not depend on the radius of the aperture. This intensity is shown in figure 4.4 for a laser beam with $w = 12$ mm, $E_0 = 1$, $\lambda = 1083$ nm and arbitrary aperture radius. The increase in intensity for lower distances z from the mirror is caused by the use of Fraunhofer diffraction, which is only valid at large distances from the mirror.

The aperture radius does influence the spread of the shadow region. For a smaller aperture the spread is larger, and the intensity distribution is influenced by the shadow for shorter distances from the mirror. The radius of the aperture has been chosen 0.5 mm. The intensity distribution at several distances from the mirror is shown. At the entrance of the Zeeman slower, $z = 3.75$ m, the intensity distribution is almost flat.

4.3 Diagnostics on slowed atomic beam

4.3.1 Problems in selecting diagnostics

To determine whether the Zeeman slower is working properly, the longitudinal velocity distribution should be known. A velocity distribution with a center velocity of 260 m/s and a small width should be measured. If a considerable number of atoms with a higher velocity are measured, this means that atoms are losing resonance during the slowing process.

Common methods for measuring the velocity distribution of an atomic beam are time-of-flight techniques. Atoms which pass a certain position will only be passed during a short time interval, other atoms will be blocked. This may be done by using a chopping wheel, or by deflecting the atomic beam with a laser. The time distribution of the signal on a remote detector gives information about the velocity distribution of the atoms.

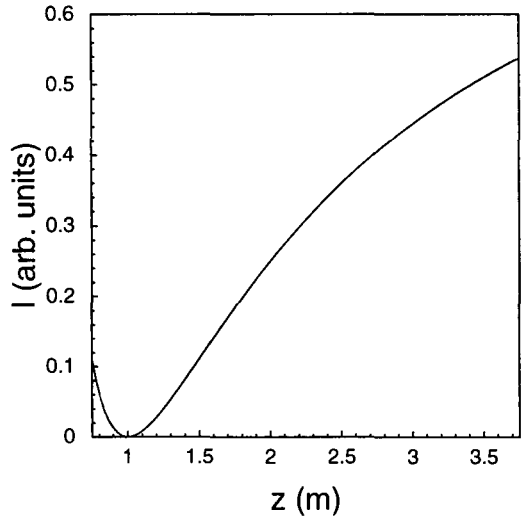

Figure 4.4: The intensity on the beam axis as a function of the distance z from the mirror. This distribution is independent of the radius of the aperture in the mirror.

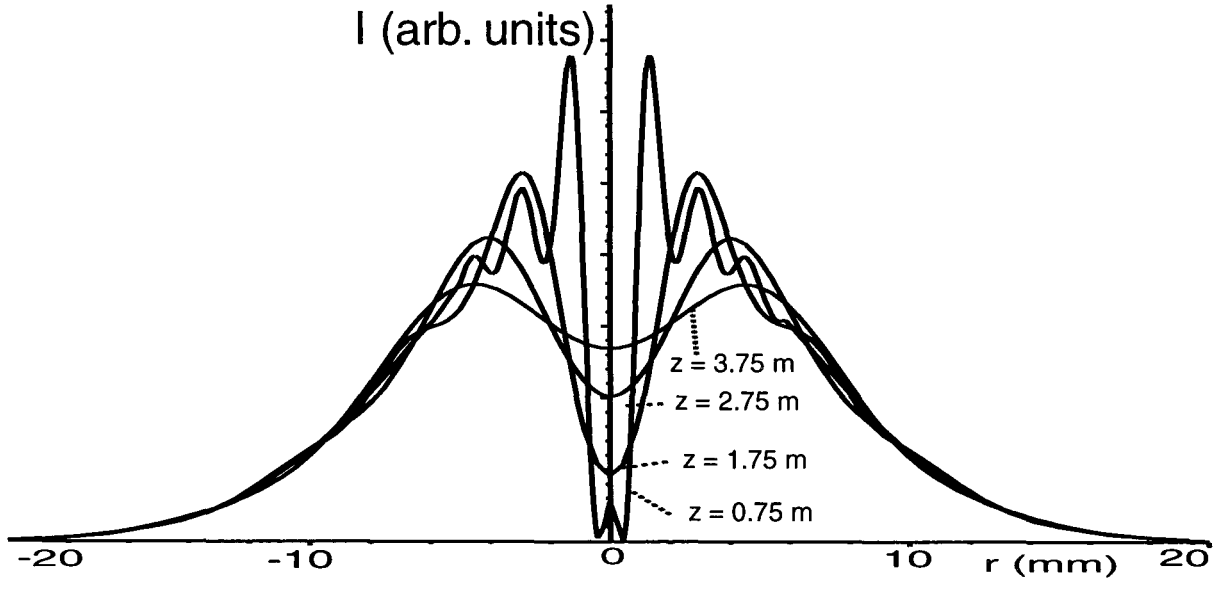

Figure 4.5: The intensity distribution at 0.75 m, 1.75 m, 2.75 m and 3.75 m from the mirror. The intensity in the center, $r = 0$ increases for larger distances from the mirror. At the beginning of the Zeeman slower, at $z = 3.75$ m, the intensity distribution is almost flat.

This method is hard to implement in the setup. If the detector is placed behind the Zeeman mirror, the distribution of a non representative group of atoms is measured. These atoms will have spent a long time in the shadow region of the aperture in the Zeeman mirror and may not be slowed to the final velocity. If the detector is placed in front of the mirror, the Zeeman laser will be blocked, unless the detector is transparent.

Another common method for measuring the velocity distribution of an atomic beam is by using fluorescence, atoms with a certain velocity are excited by a laser. The Doppler shift makes atoms within a different velocity group become resonant with the laser. The spontaneous emission of these atoms is detected within a certain solid angle. The problem is that no detectors are available which are sensitive enough to measure the very low power at the wavelength of 1083 nm.

4.3.2 Principle of absorption spectroscopy

A solution is found in using absorption spectroscopy. With this technique the absorption of the probe laser is measured directly. In this way, the loss factor of only measuring a signal in a certain solid angle is avoided.

For every detuning of the probe laser, a specific group of atoms which encounter a certain Doppler shift (and thus certain velocity component parallel to the laser beam), is resonant. When varying the detuning of the probe laser, a velocity distribution can be measured, because the number of atoms with a certain velocity component parallel to the laser beam is proportional to the absorption caused by these atoms.

A geometry in which the laser passes the atomic beam twice at the same position, but under different angles is preferable. This geometry is shown in figure 4.6(a). With a laser passing the atomic beam orthogonally a transverse velocity spread can be measured. With a laser passing the atomic beam under a different angle, e.g. 45°, the component of the velocity distribution under this angle can be measured. When the transverse velocity distribution and the velocity distribution along the 45° are known, a value for the axial velocity and axial velocity spread can be derived.

4.3.3 Geometry

The geometry shown in figure 4.6(a) could not be implemented in the existing vacuum setup. The chosen geometry is shown in figure 4.6(b). The beam traces its way back after having crossed the atomic beam twice under different angles.

The laser passing the atomic beam perpendicular is absorbed for laser detunings around $\delta = 0$ MHz. The retracing perpendicular laser will also be absorbed around this detuning. For zero detuning both lasers are resonant with the same atoms, but for a small detuning both lasers are resonant with atoms with another transverse velocity. This may cause a broadening of the absorption. When the two lasers are not perfectly aligned, i.e. there is a small angle between the two lasers, a double peaked absorption can be measured or the absorption spectrum around $\delta = 0$ MHz is broadened.

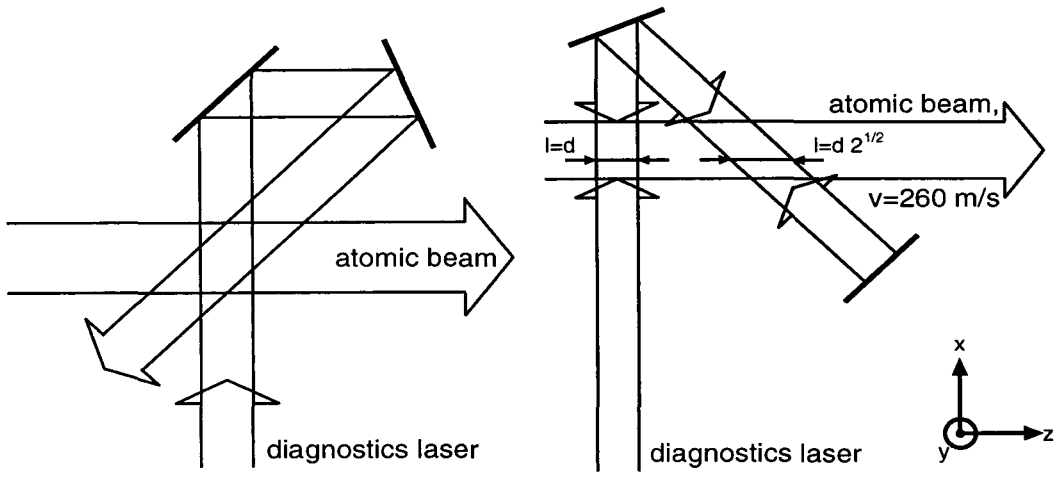

(a) *Ideal geometry.* (b) *Used geometry.*

Figure 4.6: Possible geometries for the detection laser for the velocity measurements using absorption spectroscopy.

The laser crossing the atomic beam under 45° is absorbed for values of the detuning $\delta = \frac{k}{\sqrt{2}}(v_x + v_z)$, which is about $170(2\pi)$ MHz for $k = 5.8 \times 10^6$ m^{-1}, $v_x = 0$ m/s and $v_z = 260$ m/s. The retracing laser is absorbed for $\delta = -170$ MHz. These two absorptions are thus separated and no broadening effects occur.

4.3.4 Derivation of absorption profile

4.3.4.1 General expression for the absorption

Consider a laser beam which has an interaction with an atomic beam over a length l along the atomic beam axis, labeled z. The laser beam has a square shape of dimension $d \times d$. The flux of atoms in the atomic beam is $\dot{N}$. The flux density through an surface element $\mathrm{d}x\mathrm{d}y$ at position (x, y) of atoms within a velocity interval d^3v around center velocity $\vec{v}$ is given by $\dot{N}P(x)P(y)P(\vec{v})\mathrm{d}x\mathrm{d}y\mathrm{d}^3v$, with $P(x)$, $P(y)$ and $P(\vec{v})$ distribution functions of the atomic beam flux density over the transverse coordinates and the velocity components.

The interaction time with the laser depends mainly on v_z, because in a beam $v_z \gg v_x, v_y$. The number of atoms within a certain region $\mathrm{d}z$ is given by $\dot{N}\mathrm{d}z/v_z$. The number of atoms within a velocity interval d^3v and a volume interval $\mathrm{d}^3r = \mathrm{d}x\mathrm{d}y\mathrm{d}z$ is given by

$$n(x, y, \vec{v})\mathrm{d}^3r\mathrm{d}^3v = \frac{\dot{N}P(x)P(y)P(\vec{v})}{v_z}\mathrm{d}^3r\mathrm{d}^3v, \tag{4.5}$$

The absorption of laser light with detuning Δ by atoms within a certain velocity interval d^3v around the center velocity $\vec{v}$ and within the interaction region of length l is

$$r(\Delta, \vec{v})\mathrm{d}^3r\mathrm{d}^3v = \mathrm{d}^3v \int_{-\infty}^{\infty} \mathrm{d}^3r \left\{ n(x, y, \vec{v})\rho_{ee}(y, z, \Delta - \vec{k} \cdot \vec{v})\Gamma\hbar\omega \right\}, \tag{4.6}$$

in which $\hbar\omega$ is the energy of one photon, which is in the case of the $^3S_1 \leftrightarrow ^3P_2$ transition of helium, $\hbar\omega = 1.83 \times 10^{-19}$ J, Γ is the spontaneous decay rate of the upper level and ρ_{ee} is the occupation number of the upper level, given by equation (1.6). The interaction length l is taken into account in this factor; ρ_{ee} only has a nonzero value within the interaction length. By substituting $\Delta - \vec{k} \cdot \vec{v}$ for δ, the Doppler shift is taken into account. For small intensities, $s \ll 1$, the occupation number is proportional to the saturation parameter s

$$\rho_{ee}(y, z, \Delta - \vec{k} \cdot \vec{v}) = \frac{s(y, z, \Delta - \vec{k} \cdot \vec{v})}{2} = \frac{s_0(y, z)}{2} \frac{1}{1 + \frac{4(\Delta - \vec{k} \cdot \vec{v})^2}{\Gamma^2}}. \tag{4.7}$$

The total absorption of the laser light with detuning Δ is obtained by integrating equation (4.6) over the velocity $\vec{v}$.

$$R(\Delta) = \int_{-\infty}^{\infty} \mathrm{d}^3 v \, \{r(\Delta, \vec{v})\}. \tag{4.8}$$

The laser has a certain spectral distribution around its central frequency. If this central frequency has a detuning Δ_L, the spectral distribution J can be written as $J(\Delta - \Delta_L)$. Every frequency component of the laser causes an absorption as given by equation (4.8), assuming the frequency components in the spectral distribution to have no mutual coherence (i.e. the broadening of the laser spectrum is caused by stochastic noise). The total absorption of the laser with a certain detuning Δ_L is obtained by integrating equation (4.8) over all detunings Δ with the spectral distribution of the laser as a weight function

$$A(\Delta_L) = \int_{-\infty}^{\infty} \mathrm{d}\Delta \, \{J(\Delta - \Delta_L) R(\Delta)\}. \tag{4.9}$$

The integration over Δ is a convolution of the Lorentz lineform of the atomic transition in ρ_{ee} and the spectral distribution of the laser $J(\Delta - \Delta_L)$. This convolution or overlap integral is known if the spectral distribution of the laser is known. Using equation (4.7), the overlap integral is

$$C(\vec{k} \cdot \vec{v} - \Delta_L) = \int_{-\infty}^{\infty} \mathrm{d}\Delta \left\{ \frac{1}{1 + \frac{4(\Delta - \vec{k} \cdot \vec{v})^2}{\Gamma^2}} J(\Delta - \Delta_L) \right\}. \tag{4.10}$$

Equation (4.9) now takes the form, using equations (4.10) and (4.5) - (4.8)

$$A(\Delta_L) = \frac{\dot{N}\Gamma\hbar\omega}{2} \int_{-\infty}^{\infty} \mathrm{d}x \, \{P(x)\} \int_{-\infty}^{\infty} \mathrm{d}y \int_{-\infty}^{\infty} \mathrm{d}z \, \{P(y) s_0(y, z)\} \int_{-\infty}^{\infty} \mathrm{d}^3 v \left\{ \frac{P(\vec{v}) C(\vec{k} \cdot \vec{v} - \Delta_L)}{v_z} \right\}. \tag{4.11}$$

The integration over x equals unity. Both $P(y)$ and $s_0(y, z)$ are positive functions and symmetrically around 0 for the y- and the z-coordinate. The saturation parameter $s_0(y, z)$ can be replaced by some average value s_0 over the interaction area. The integration over y

and z may now only be taken over the interaction area. The integration over z now equals the length of the interaction area l. The integration of $P(y)$ represents the overlap between the laser beam and the atomic beam in the y-direction (the overlap will be smaller than 1 if the laser beam is narrower than the atomic beam). It is replaced by an overlap factor W_y:

$$\int_{-\infty}^{\infty} \mathrm{d}y \int_{-\infty}^{\infty} \mathrm{d}z \left\{P(y)s_0(y,z)\right\} \equiv s_0 l W_y. \tag{4.12}$$

By substituting this value in equation (4.11) we get

$$A(\Delta_L) = \frac{\dot{N} W_y \Gamma \hbar \omega s_0 l}{2} \int_{-\infty}^{\infty} \mathrm{d}^3 v \left\{ \frac{P(\vec{v}) C(\vec{k}\cdot\vec{v} - \Delta_L)}{v_z} \right\}. \tag{4.13}$$

The total power $\mathcal{P}$ of the probe laser equals

$$\mathcal{P} = s_0 d^2 I_0. \tag{4.14}$$

The relative absorption $A/\mathcal{P}$ of the probe laser is independent of the intensity of the probe laser, as long as the intensity is very small, $s_0 \ll 1$

$$\frac{A(\Delta_L)}{\mathcal{P}} = \frac{\dot{N} W_y \Gamma \hbar \omega}{2 I_0} \frac{l}{d^2} \int_{-\infty}^{\infty} \mathrm{d}^3 v \left\{ \frac{P(\vec{v}) C(\vec{k}\cdot\vec{v} - \Delta_L)}{v_z} \right\}. \tag{4.15}$$

4.3.4.2 Absorption of orthogonal laser beam

The Doppler detuning $\vec{k}\cdot\vec{v}$ now depends on the transverse velocity component of the atoms, because the laser beam is orthogonal to the atomic beam axis. The axial velocity determines the interaction time of an atom with the laser. The interaction length l is equal to the width of the laser d. Equation (4.15) now becomes

$$\frac{A(\Delta_L)}{\mathcal{P}} = \frac{\dot{N} W_y \Gamma \hbar \omega}{2 I_0 d} \int_{-\infty}^{\infty} \mathrm{d}v_z \left\{ \frac{P(v_z)}{v_z} \right\} \int_{-\infty}^{\infty} \mathrm{d}v_x \left\{P(v_x) C(k v_x - \Delta_L)\right\}. \tag{4.16}$$

To be able to interpret the measurement qualitatively, the longitudinal velocity distribution must be known. If this is not the case, the integral over v_z can be considered to be an unknown scaling factor. The transverse velocity spread can still be determined if the transverse and longitudinal velocity distributions are uncorrelated, as has been assumed in equation (4.5).

If the axial velocity spread is small in comparison to the mean axial velocity $\langle v_z \rangle$ of the atomic beam, the velocity v_z in the denominator of equation (4.16) can be considered constant and can be taken out of the integral

$$\frac{A(\Delta_L)}{\mathcal{P}} = \frac{\dot{N} W_y \Gamma \hbar \omega}{2 I_0 d \langle v_z \rangle} \int_{-\infty}^{\infty} \mathrm{d}v_x \left\{P(v_x) C(k v_x - \Delta_L)\right\}. \tag{4.17}$$

The total relative absorption in this case is a direct measure of the number of the number of slowed particles, because the interaction time of all particles with the laser is similar.

4.3.4.3 Absorption of 45° beam

The interaction length l is $\sqrt{2}$ times the width of the laser beam d, because the laser beam is under an angle of 45° with the atomic beam axis. Both the transverse and the longitudinal velocity distributions contribute to the measured velocity distribution, according to

$$v_{\parallel} = (v_x + v_z)/\sqrt{2}, \tag{4.18}$$

with $v_{\parallel}$ the velocity component along the 45° laser. The factor v_z in the denominator of equation (4.13) can be replaced by $\sqrt{2}v_{\parallel}$, by using equation (4.18) and $v_x \ll v_z$. The interaction length now is $d\sqrt{2}$. Equation (4.15) now becomes

$$\frac{A(\Delta_L)}{\mathcal{P}} = \frac{\dot{N}W_y\Gamma\hbar\omega\sqrt{2}}{2I_0 d}\int_{-\infty}^{\infty} \mathrm{d}v_{\parallel}\left\{\frac{P(v_{\parallel})C(kv_{\parallel}-\Delta_L)}{\sqrt{2}v_{\parallel}}\right\}. \tag{4.19}$$

Using the measured values for the velocity spread $(\Delta v_{\parallel})_{FWHM}$ parallel to the 45° laser and the transverse velocity spread $(\Delta v_x)_{FWHM}$, the axial velocity spread can be calculated to be

$$(\Delta v_z)_{FWHM} = \sqrt{2(\Delta v_{\parallel})^2_{FWHM} - (\Delta v_x)^2_{FWHM}}. \tag{4.20}$$

4.4 Absorption spectroscopy experiments

4.4.1 Estimate of the absorption

Consider the case with the following realistic parameters. With the flux of atoms $\dot{N}$ in the slowed atomic beam, with velocity $\langle v_z\rangle$ and with the width of the of the laser d, the number of atoms resonant with the laser is maximally $\dot{N}d/v$. The fraction of these atoms which spontaneously emits a photon is $s_0 f\Gamma/2$, with Γ the spontaneous decay rate of the atoms, s_0 the saturation parameter, corrected by the fraction f of the laser power which is effectively used. This fraction is previously mentioned in section 3.1.3. Each emitted photon has an energy of $\hbar\omega$. The absorbed power A is thus

$$A = \frac{\dot{N}d}{\langle v_z\rangle}\frac{s_0 f}{2}\hbar\omega. \tag{4.21}$$

With $\dot{N}$ of the order of the flux of atoms in the collimated beam, so $\dot{N} \approx 10^{11}$ s^{-1}, with $\langle v_z\rangle = 260$ m/s, $s_0 = 0.1$, $f = 0.46$, $\Gamma = 10.22 \times 10^6$ s^{-1} and $\hbar\omega = 1.83 \times 10^{-19}$ J, the estimated absorption is $A = 0.33$ μW

The total power of the laser beam is

$$P = s_0 I_{0,\pi} d^2, \tag{4.22}$$

in which s_0 is the saturation parameter and $I_{0,\pi}$ is the saturation intensity for linearly polarized light. The total energy in the laser beam is $P = 111$ μW. The relative absorption is thus about 3×10^{-3}.

4.4.2 Experimental setup

The absorption is very low, in the order of a microwatt. The changes in laser power when detuning are in the same order of magnitude. Therefore the laser frequency is modulated and the transmission signal is measured phase sensitively. A schematic overview of the absorption setup is shown in figure 4.8.

The detuning of the laser is changed by changing the current through the laser. The frequency dependence of the laser on the current through the laser is determined by looking at the difference in current between the $^3S_1 \leftrightarrow ^3P_1$ transition and the $^3S_1 \leftrightarrow ^3P_2$ transition in a saturated absorption setup, the same method as used for the collimator laser and is $490(2\pi)$ MHz/mA. The frequency at which the laser is at resonance with the $^3S_1 \leftrightarrow ^3P_2$ transition is determined by looking at the saturated absorption signal. The current through the laser is modulated using the 1025 Hz internal oscillator of the phase sensitive amplifier used.

The laser setup is schematically shown in figure 4.7. The laser used is a DBR diodelaser (appendix E). The laser is isolated from any optical feedback by using an optical isolator (Conoptics, model 715), with two lenses, with a focal distance of 100 mm, to focus through the isolator. The polarization is made vertical using a half wave plate. Behind the half wave plate some power is reflected into a beam for saturated absorption spectroscopy, using a beamsplitter consisting of a thick glass plate (BK7, optically flat over $\lambda/10$). The laser power can be easily varied by adjusting the half wave plate in front of the polarizer. Using an anamorphic prism pair the beam shape is made circular. Finally the beam size is increased using two lenses. By using a rectangular aperture with a dimension of 20 mm, the beam size is defined. The laser now enters the interaction region and some power is absorbed by the atomic beam. The absorbed laser beam is focused on the detector using two lenses.

The laser frequency is modulated by injecting a modulating current into the laserdiode. This current is created by putting a voltage over a 12.7 kΩ resistance. The voltage is the 100 times attenuated voltage of the 1025 Hz internal oscillator of the phase sensitive amplifier, which has an amplitude of 3 V. The modulation depth is thus about 1.15 MHz.

An AC coupled detector, discussed in appendix F.3, is used to measure the laser power absorption. This detector has a high pass filter with a cut-off frequency of 160 Hz. The absorption can thus still be detected, because it is modulated with 1025 Hz. Also the DC signal can be measured to obtain a value for the total laser power. The AC signal is 100 times amplified and then multiplied with the signal of the internal oscillator. After passing through a low pass filter, the signal is proportional to the first derivative of the absorption. this signal is measured.

The detuning of the laser is varied by injecting a second current in the laser by adding a voltage from a 10 V DAC to the voltage over the resistance of 12.7 kΩ. A maximum detuning of $408(2\pi)$ MHz can be reached.

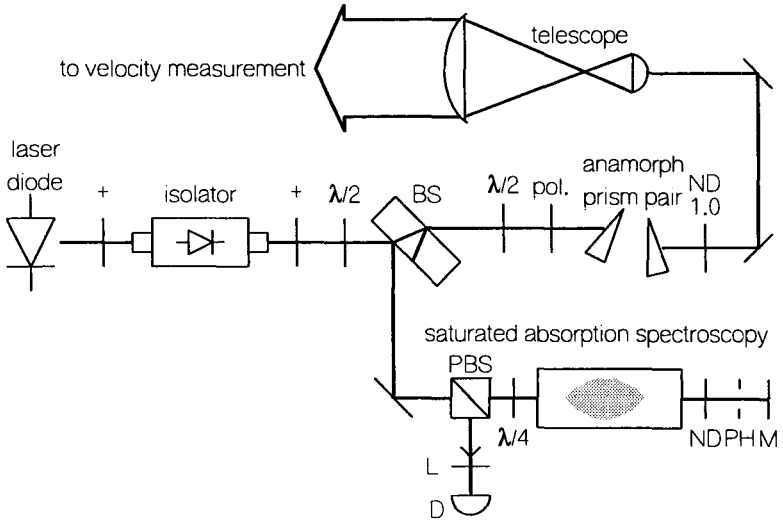

Figure 4.7: Schematic overview of the laser setup for the velocity measurement.

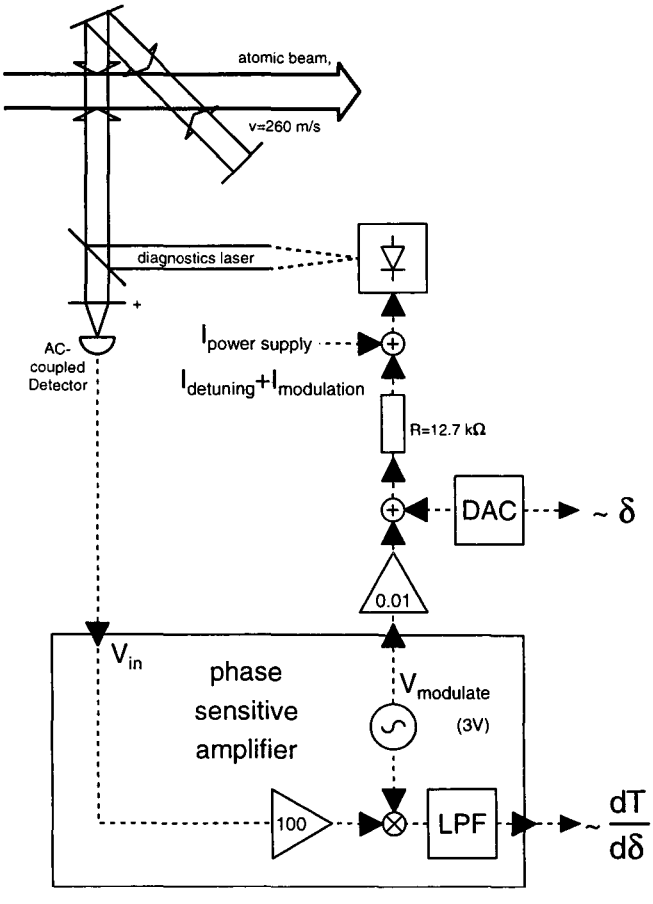

Figure 4.8: Schematic overview of the setup for measuring the velocity distribution of the slow atoms.

4.4.3 Interpretation of absorption spectra

The measured signal M is proportional to the derivative $\mathrm{d}A/\mathrm{d}I$ of the absorption A to the laser current I. To derive the actual absorption from this measured signal is by integrating the measured derivatives

$$A = \int \frac{\mathrm{d}A}{\mathrm{d}I}\mathrm{d}I \approx \sum_i \left(\frac{\Delta A}{\Delta I}\right)_i \Delta' I, \tag{4.23}$$

in which the final step is made to express the integral in a sum over the discrete current steps $\Delta' I$. The derivative is expressed in values for the amplitude of the current modulation ΔI and the amplitude of the AC part of the absorption signal ΔA.

The amplitude of the current modulation ΔI can be derived from the amplitude of the voltage modulation of the internal oscillator of the phase sensitive amplifier $\Delta V = 3$ V by

$$\Delta I = \frac{1}{100R}\Delta V, \tag{4.24}$$

because the voltage of the internal oscillator is first attenuated with a factor 100 and is then made into an injection current over a resistance R of 12.7 kΩ.

The amplitude of the absorption ΔA can be derived from the measured signal M of the low pass filter of the phase sensitive amplifier by

$$\Delta A = \frac{\pi}{2}\frac{1}{100}\left(M - M_0\right), \tag{4.25}$$

because it is first amplified with a factor 100. The factor $\pi/2$ follows from the average value of the product of the amplified detector signal and a square wave with amplitude 1 from the internal oscillator. The term M_0 is an offset in the phase sensitive amplifier which has to be subtracted to give the real value for the amplitude of the AC component of the absorption signal.

To get a value for the relative absorption, the absorption A must be divided by the total power $\mathcal{P}$, which can also be measured behind the first amplification step of the AC coupled detector:

$$\frac{A}{\mathcal{P}} = \frac{1}{\mathcal{P}}\sum_i \frac{\pi}{2}\frac{R}{\Delta V}\left(M_i - M_0\right)\Delta' I. \tag{4.26}$$

The detuning of the laser in the measurement data is in units of current, because the transfer function of the DAC and the resistance, used to create an injection current, is known. The offset of this current from the atomic transition is determined using a saturated absorption spectroscopy setup. Using the frequency current relation of the laser used for the absorption spectroscopy, $\mathrm{d}\omega/\mathrm{d}I = 490(2\pi)$ MHz/mA, a value for the frequency of the laser can be derived.

Information about the center velocity and the velocity spread of the atomic beam is achieved from these absorption spectra by comparison with calculated spectra, calculated

using equation (4.17) or (4.19). In these calculations a Gaussian velocity distribution is assumed. When calculating the overlap integral (4.10) a Gaussian distribution with a FWHM of 3 MHZ is assumed for the spectral distribution of the laser. By varying the values for $\dot{N}W_y$, the center velocity and velocity spread of the velocity distribution, the calculated spectra can be fitted to the measured spectra. By interpreting $\dot{N}W_y$ as the flux of particles, a lower limit for the flux is derived, because $W_y < 1$, but is not known exactly.

4.4.4 Measurements using absorption spectroscopy

4.4.4.1 Measurements on collimated beam

By doing absorption spectroscopy measurements with the 90° lasers on the collimated beam, without the Zeeman slower operating, information about the transverse velocity spread of the atomic beam can be obtained. These values can be compared with the values obtained from the measurements with the wire scanners. Also a value for the number of particles in this beam can be derived. Absorption spectroscopy measurements with the 45° lasers turned out not to be achievable, because the absorption was too low, due to the high velocity of the atoms.

In figure 4.9(a) the experimental data with only the collimator working is shown. In figure 4.9(b) the absorption spectrum, calculated from the measurement is shown. From figure 4.9(a) the offset in the measurement, mentioned in paragraph 4.4.3, is clear. Also a two-peaked structure is visible. This means that the two orthogonal laser beams are not perfectly overlapping, i.e. there is a small angle between these two lasers. Striking in figure 4.9(b) is the residual offset of the absorption spectrum on the right side of the spectrum. This effect will be further discussed in paragraph 4.4.4.3.

The two peaked structure has been reproduced by fitting the sum of two Gaussian profiles. These profiles are also shown in figure 4.9(b), including the resulting two peaked structure. The peaks have a FWHM of 8 MHz and are 8 MHz apart. With an average velocity of the atoms in the atomic beam of 1100 m/s, this gives a misalignment of the two orthogonal lasers of 8 mrad. In terms of transverse velocity, the two peaks are 8.7 m/s apart.

The two Gaussian profiles have been fitted with equation (4.17). The FWHM of the beam at this position is about half the diameter of the laser beam, as follows from the measurements with the wire scanners. Therefore the factor W_y in equation (4.17) will equal unity, all atoms are taken into account in the absorption spectroscopy measurement.

The derived flux of particles in the atomic beam is 2.2×10^{11} He*s^{-1}. This number is accurate to within 20%, because a single longitudinal velocity of $v_z = 1100$ m/s was chosen to perform a fit with equation (4.17), whereas the longitudinal velocity is distributed over a wide spectrum. The flux measured with the wire scanners was 1.6×10^{11} He*s^{-1} within the FWHM of the beam profile. These values are of the same order, especially if the uncertainty in the source intensity is taken into account.

The transverse velocity spread of the atoms is 6 m/s. This is comparable to a residual divergence of the atomic beam of 2.3 mrad for an atomic beam with a average velocity of

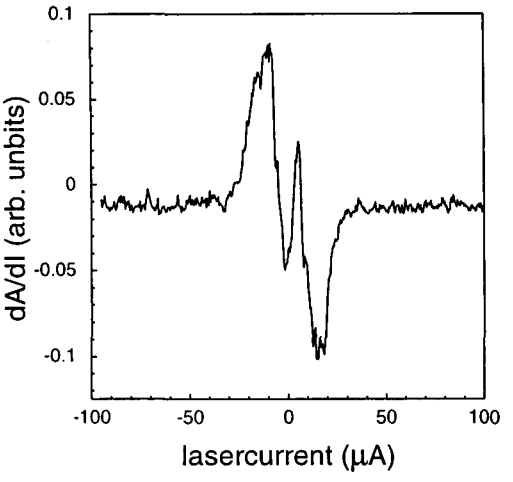

(a) *Experimental data.*

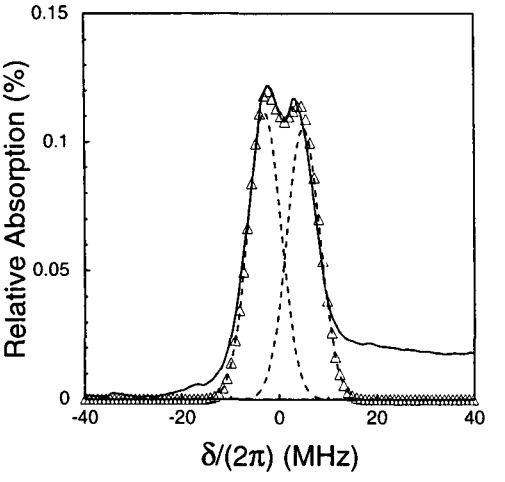

(b) *Absorption spectrum (straight lines) and fitted spectra for the two absorption peaks (dotted lines and △).*

Figure 4.9: The experimental data and the resulting absorption spectrum of a collimated beam with the Zeeman slower turned off, measured with the 90° *lasers.*

1300 m/s. Measurements with the wire scanners a residual divergence of 1.0 mrad. The residual divergence determined using absorption spectroscopy is about a factor two larger than the estimate based on the beam profile measurements. The estimate is probably too high due to the offset of the absorption spectrum on the right side of the spectrum. The fit parameters had to be changed manually to obtain the best fit result, which can also cause an inaccuracy of the estimates.

4.4.4.2 Absorption of the 90° lasers

In figure 4.10 the absorption spectrum of the 90° lasers with the Zeeman slower turned on is shown. Also this spectrum consists of two peaks, but these are indistinguishable due to the larger width of the peaks. This absorption spectrum is fitted with equation (4.17) using a Gaussian velocity distribution. This resulted in a flux of 2.2×10^{11} He^*s^{-1} and a velocity spread of 14 m/s FWHM. The flux must be divided by two, because the spectrum consists of two peaks, resulting in a flux of 1.1×10^{11} He^*s^{-1}.

The obtained flux only accounts for the atoms within the detection laser. The detection laser only has a dimension of 20 mm and the slowing laser has a diameter of 30 mm. The simulated diameter of the atomic beam at the end of the Zeeman slower is 45 mm FWHM, see [KNO98]. From these parameters it is estimated that approximately 80% of the total number of slowed atoms is measured. The influence of not slowed atoms on these measurements is very low, because their contribution to the absorption is very small due

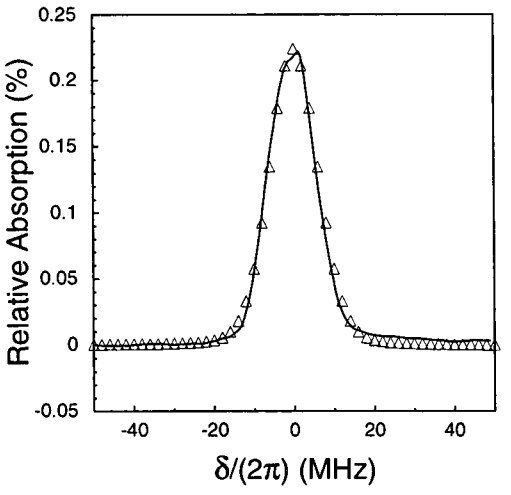

Figure 4.10: Absorption spectrum of the 90° lasers (-) and the fitted spectrum (△) for an atomic beam with longitudinal velocity of 255 m/s.

to their high velocity.

The 8 mrad misalignment between the two orthogonal laser causes a splitting of the two absorption peaks of 1.9 MHz in laser detuning, or 2 m/s transverse velocity. The velocity spread must be corrected for this broadening effect. By simulating two Gaussian profiles, 2 m/s apart, an original velocity spread of 13.5 m/s FWHM is derived.

This transverse velocity spread is indeed larger than the transverse velocity spread of the atomic beam with just the collimator working. The increase is caused by the random effect of the spontaneous emissions and is therefore proportional to the square root of the number of absorbed photons n, about 11000. The increase in transverse velocity spread derived using this rule of thumb is about $\sqrt{n}\frac{\hbar k}{m} = 9.6$ m/s. This is approximately the observed increase in transverse velocity.

4.4.4.3 Absorption of the 45° lasers

For the absorption spectroscopy under 45°, two laser beams are available, a beam copropagating with the atomic beam and the retracing beam. Both beams should give the same results. There is no interference between the two lasers, due to large frequency difference for which they are resonant with the atomic beam.

In figure 4.11 two absorption measurements are shown for the copropagating laser. Both absorption spectra have a maximum value for a detuning of $166(2\pi)$ MHz, which corresponds with a longitudinal velocity of 255 m/s. On the right of the spectrum in figure 4.11(a) the absorption does not decrease to zero. This might indicate that particles are losing resonance at the end of the slowing process and leave the Zeeman slower with a too high velocity. For higher velocities the absorption spectrum should decrease to zero.

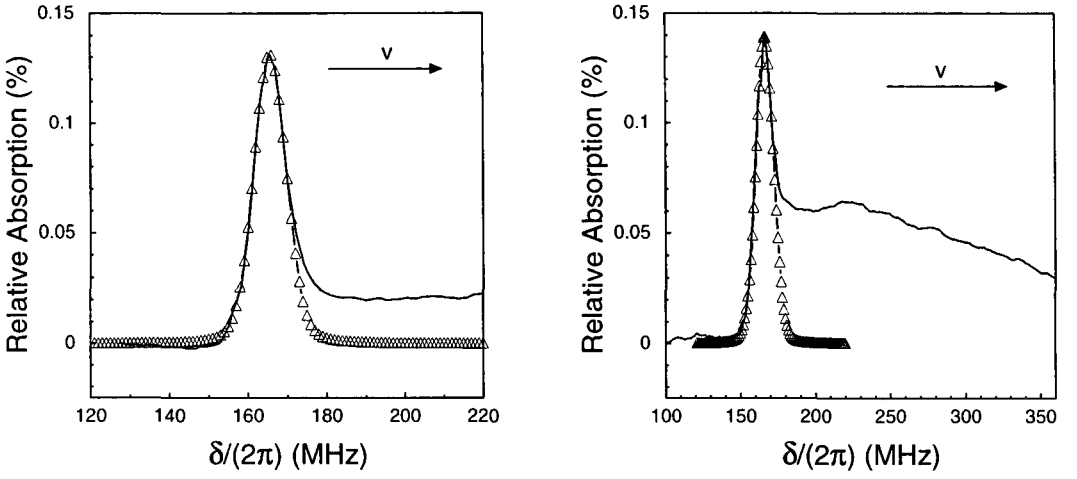

Figure 4.11: Absorption spectra measured with the 45° laser (-) and the fitted spectra (△), using equation (4.19).

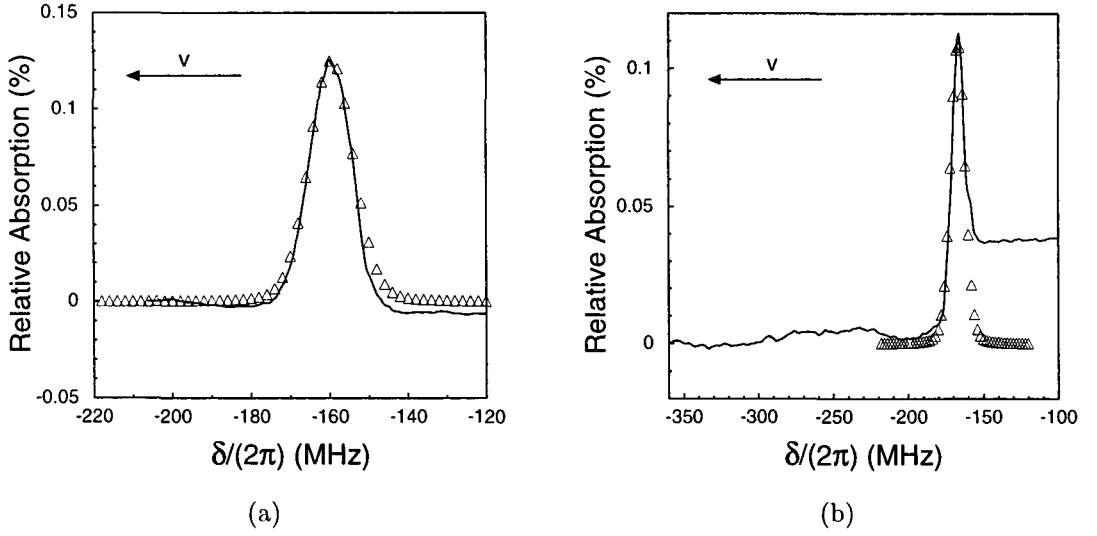

Figure 4.12: Absorption spectra measured with the retracing 45° laser (-) and the fitted spectra (△), using equation (4.19).

measurement shown in figure	$\delta/(2\pi)$ (MHz)	fitted velocity distribution parameters			longitudinal velocity spread (m/s)
		center velocity (m/s)	flux (10^{10} He*s^{-1})	FWHM (m/s)	
4.11(a)	165.6	179.5	6	9	-
4.11(b)	166.7	180.5	9	13.5	13.5
4.12(a)	-160.0	173	7	13	12.5
4.12(b)	-166.0	181	6	11	7.7

Table 4.1: Several parameters of the absorption spectra of the 45° lasers and of the fitted velocity distributions.

The spectrum in figure 4.11(b) measures the absorption for longitudinal velocities up to about 380 m/s. The tail of possible fast particles is even higher in this spectrum, although both measurements were performed under identical conditions. The absorption decreases for higher velocities. This should already happen because of the smaller influence on the absorption due to the shorter interaction time with the detection laser for a particle with a higher velocity.

The absorption peaks of the fully slowed particles are fitted using equation (4.19). The fitting parameters for the velocity distribution are given in table 4.1. The flux needed to fit the main absorption peak in the spectra already accounts for for all the atoms in the atomic beam. When the high velocity tail of the spectrum is actually caused by absorption of laser light by faster atoms, the flux of particles in the atomic beam needed to explain this spectrum is much higher than the flux in the collimated atomic beam, which is about 1.5×10^{11} He*s^{-1}. The assumption that the tail on the higher velocity side of the spectra is actually caused by faster atoms is thus not plausible.

The absorption peaks of the retracing 45° laser are shown in figure 4.12. It must be noticed that the graphs must be interpreted the other way round; the contribution of particles with higher longitudinal velocities is on the left of the spectrum. The absorption to the right of the main peak in the spectrum, i.e. the absorption of slower atoms, should be shifted to zero, because the atoms can not be too slow. The spectrum in figure 4.12(a) has only a very small tail for higher velocities. The spectrum in figure 4.12(b) even has a negative tail on the higher velocity side of the spectrum. These measurements confirm the assumption that the tail is not caused by faster atoms in the atomic beam.

Possible causes for the offset on the high velocity side of the absorption spectra can be sought in the process of obtaining the spectra from the measured derivative signal. Rounding errors in the measurement procedure of the derivatives, or rounding errors in the integration process to obtain the absorption spectra, may cause arbitrary offsets.

The offset can also be caused by drifts or frequency jumps of both the slowing laser and the detection laser. If the slowing laser jumps in frequency, the final velocity of the atomic beam is changed. Therefore parts of the velocity spectrum are not measured with the absorption spectroscopy, or are measured twice. The same holds for any frequency jumps of the detection laser. The effect for this last laser is probably larger, because it

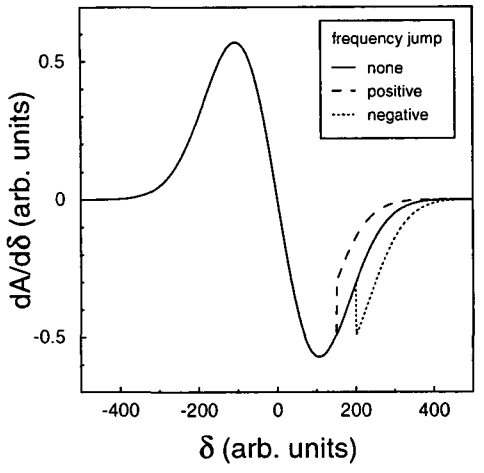

(a) *Simulated measurement data with frequency jumps of the detection laser.*

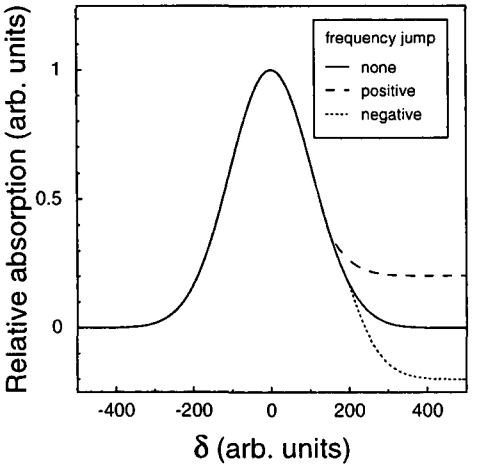

(b) *Derived absorption spectra.*

Figure 4.13: A frequency jump of the detection laser - positive or negative - can cause a tail in the absorption spectrum, which is based on a measurement of the the derivative of the absorption profile.

is an unstabilized laser. The duration of the measurements of ten to twenty minutes also increases the influence of these effects.

Consider a simulated measurement of the derivative of the absorption spectrum as shown by the full line in figure 4.13(a). The absorption spectrum based on this measurement is shown in figure 4.13(b). We now consider a frequency jump of the detection laser on the flank for decreasing absorption, as shown by the dashed and dotted lines in figure 4.13(a). The measurement with a negative frequency jump is shown by the dots, with a positive frequency jump by the dashes. In figure 4.13(b) is shown that the resulting absorption spectrum shows a tail similar to the tails visible in the actual measurements. The tail is positive for a positive frequency jump and negative for a negative frequency jump. The behaviour for a frequency jump on the flank for increasing absorption of the absorption spectrum would be reverse. Effects similar to these are probably the cause of the tail visible in the derived absorption spectra.

The final velocity of the atomic beam is 255 m/s with a flux of slow atoms of about 7×10^{10} He^*s^{-1}. The velocity spread along the 45° laser is about 13 m/s. Using the transverse velocity spread of 13.5 m/s, derived in the previous section, the longitudinal velocity spread can be calculated with equation (4.20). The longitudinal velocity spread is about $(\Delta v_z)_{FWHM} = 12.5$ m/s. There probably will be a contribution of faster atoms, but by using absorption spectroscopy and by measuring phase sensitively, no estimate of the amount of faster atoms can be made.

4.5 Conclusions

The Zeeman slowing section seems to be functioning properly. A flux of 7×10^{10} He^*s^{-1} is slowed down to the final velocity of 255 m/s for an input flux of about 1.5×10^{11} He^*s^{-1}. The velocity spread is 12.5 m/s, which is well within the 15 m/s mentioned in the introduction. The transverse velocity spread was determined to be 13.5 m/s FWHM.

The absorption spectroscopy technique used to measure the velocity distribution was suitable for a first indication of the velocity distribution. Due to the low absorbed laser powers it was necessary to measure the derivative of the absorption. Errors in the derivative signal, probably caused by frequency jumps of the detection laser, caused a virtual tail in the absorption spectrum. Therefore it is impossible to determine whether there are faster atoms leaving the Zeeman slower.

It is recommended to perform a more accurate measurement of the velocity distribution when the lens and the compressor are working. Then time-of-flight techniques can be performed to measure the velocity distribution of the atoms which will finally traverse the cavity.

The absorption spectroscopy techniques were also used to determine the characteristics of the collimated atomic beam. These resulted in residual divergence of 2.3 mrad, a higher estimate than obtained from the beam profile measurements. This can be attributed to the inaccuracy of the fit procedure of the absorption profiles.

Chapter 5

Concluding remarks

The laser-cooling elements used for the preparation of a beam of atomic helium have been set up and tested, with emphasis on the collimator and the Zeeman slower. The performance obtained so far is sufficient for the application of the beam in quantum optics experiments.

The source is performing perfectly. The center line intensity of 4×10^{14} $He^*s^{-1}sr^{-1}$ is a factor of two better than the expected performance of such source. Although its intensity may vary in time, it has never showed a drastic decrease in signal.

The best performance of the collimator was obtained by using a plane wavefront and a large detuning of the collimator laser of $-7(2\pi)$ MHz. A flux of 1.5×10^{11} He^*s^{-1} was captured in a collimated beam with a residual divergence of (0.7 ± 0.1) mrad, defined as the angle between the beam axis and the line through the HWHM of the atomic beam profiles at different positions.

Increasing the capture angle of the collimator seems feasible by using a curved wavefront. To achieve this, the quality of the wavefront should be improved by replacing the machined lens of the telescope by a lens of better quality. Also narrowing the linewidth of the collimator laser could help, because the collimator could then be operated with a smaller detuning.

The Zeeman slower slows 50 - 70% of the beam flux to the final velocity of approximately 255 m/s with a velocity spread of 12.5 m/s. The beam is analysed using absorption spectroscopy where the derivative of the absorption spectrum is measured. The velocity spread is within the maximum spread of 15 m/s, as mentioned in the introduction.

Also no value for the number of faster atoms leaving the Zeeman slower could be determined, due to the detection method. In the future, when the compressor section is operational, highly accurate values for the velocity distribution can be determined using the time-of-flight technique.

Bibliography

[BEY93] H.C.W. Beyerink, P. v.d. Straten, H. Rudolph, *Lasercooling: Principle and Practice*, lecture notes, TUE, VDF/NO 93-10.

[BRU89] M. Brugmans, *Diodelaser: lijnbreedte, tweede versie stroombron en behuizing, snelle bepaling van de golflengte*, internal report, TUE, VDF/NO 89-04.

[GOR80] J.P Gordon, A. Ashkin, *Motion of atoms in a radiation trap*, Phys. Rev. A **21**, 1606 (1980).

[HAB97] B. Habets, *Some Aspects of a New Metastable Helium Beam Set-Up for Quantum and Atom Optics Experiments*, master of science thesis, TUE, VDF/NO 97-11.

[JON98] J. de Jong, *Ringdown Metingen aan een Hoge Finesse Optische Trilholte*, internal report, TUE, VDF/NO 98-08.

[KNO98] R.M.S. Knops, *Quantum Optics with a Cold Helium Beam*, PhD thesis.

[MAS97] H.C. Mastwijk, *Cold Collisions of Metastable Helium Atoms*, PhD thesis.

[PED93] F.L. Pedrotti, L.S. Pedrotti, *Introduction to Optics*, 2nd edition, Prentice-Hall.

[REI98] W. Reijnen, *Frequentiestabilisatie van een diodelaser m.b.v. een extern magneetveld*, internal report, TUE, VDF/NO 98-04

[SHI94] D. Shiner, R. Dixson, P. Zhao, *Precise Measurement of the Lamb Shift and Fine Structure of the 2S-2P Transition in Triplet Helium*, Phys. Rev. Lett. **72**, 1802 (1994).

Appendix A

Constants

Some useful physical constants				
Boltzmann's constant	k	1.38062	$\times 10^{-23}$	J K^{-1}
Planck's constant	h	6.62620	$\times 10^{-34}$	J s
Dirac's constant	$\hbar = \frac{h}{2\pi}$	1.05459	$\times 10^{-34}$	J s
Bohrmagneton	μ_B	9.2741	$\times 10^{-24}$	A m^2
speed of light in vacuum	c	2.9979246	$\times 10^{8}$	m s^{-1}
elementary charge	e	1.6021892	$\times 10^{-19}$	C
atomic mass unit	u	1.66057	$\times 10^{-27}$	kg
restmass proton	m_p	1.67261	$\times 10^{-27}$	kg
restmass electron	m_e	9.10956	$\times 10^{-31}$	kg

Characteristic values of metastable helium, $^3S_1 \leftrightarrow ^3P_2$ transition				
mass	m	6.642	$\times 10^{-27}$	kg
viscosity	η	18.6	$\times 10^{-6}$	Pa's
wavelength	λ	1083.034		nm
wavevector	k	5.80	$\times 10^{6}$	m^{-1}
angular frequency	ω	1.74 (2π)	$\times 10^{15}$	s^{-1}
decay rate	Γ	1.6 (2π)	$\times 10^{6}$	s^{-1}
saturation parameter σ light	$I_{0\sigma}$	1.67		μW mm^{-2}
saturation parameter π light	$I_{0\pi}$	2.78		μW mm^{-2}
one photon recoil velocity	$\frac{\hbar k}{m}$	0.092		m s^{-1}
doppler limit	v_D	0.28		m s^{-1}
maximum force	F_{max}	3.13	$\times 10^{-21}$	N
Zeeman shift for σ light	$d\omega/dB$	1.399 (2π)	$\times 10^{10}$	Hz T^{-1}
internal energy of $^3S_1$ state		21.03		eV

Appendix B

Source

The source used in the setup is a supersonic expansion discharge source, as schematically shown in figure B.1. The nozzle is made from boron-nitride and has a diameter of 0.1 mm. The skimmer has a diameter of 1 mm.

Some helium atoms are excited to the metastable 2^3S_1 level by collisions with electrons from the discharge. The discharge is drawn from the cathode through the nozzle to the skimmer. The source is cooled with liquid nitrogen which reduces the effective source temperature and therefore the velocity of the atoms in the expansion.

Time of flight measurements of the metastable helium atoms, described in [KNO98], show an axial velocity distribution centered at 1300 m/s with a FWHM $\Delta v = 600$ m/s. Using Boltzmann's law the temperature T of the atoms follows from

$$T = \frac{mv^2}{8k \ln 2}, \tag{B.1}$$

with v the velocity of the atoms, k Boltzmann's constant and m the mass of a helium atom. Using the measured velocity, a temperature of $T = 150$ K follows for the atoms. The measurement of the velocity distribution of the source was performed with a discharge current of about 10 mA.

The discharge of the source normally operates at a current of about 5.5 mA and a voltage of about 700 V. In section 3.3.2.3 a center line intensity of 4×10^{14} $He^*s^{-1}sr^{-1}$ was measured.

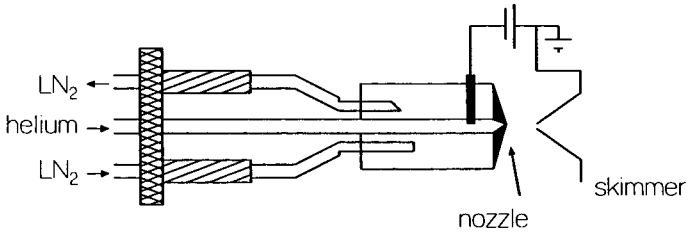

Figure B.1: Schematic representation of the source.

The flow of helium atoms can be estimated from the gas flow of the source. The gas flows from a region of constant pressure $p_0 \approx 270$ Torr (this was about 350 Torr for in the measurement of the velocity distribution) through a capillary with a radius R of 0.1 mm and a length l of 100 mm to the gas inlet of the source. The pressure in the source chamber is $p_1 \approx 4 \times 10^{-4}$ mbar. The flow through the capillary is laminar and the volume displacement Φ can thus be described by Poiseuille's law

$$\Phi = \frac{\pi}{8\mu}(p_0 - p_1)\frac{R^4}{l}, \tag{B.2}$$

in which μ is the viscosity of the gas used. The source pressure p_1 can be neglected with respect to p_0. Using this capillary the volume displacement is regulated.

Making use of the ideal gas law $pV = NkT$, with k Boltzmann's constant and N the number of particles in a volume V at temperature T and pressure p, equation (B.2) can be written as a flux $\dot{N}$ of particles

$$\dot{N} = \frac{\pi p_0^2}{8\eta kT}\frac{R^4}{l}. \tag{B.3}$$

When the effects of the skimmer are neglected and only the nozzle is considered, the source intensity $I(0)$ is given by the expansion geometry and is given by

$$I(0) = \frac{2}{\pi}\dot{N} = \frac{p_0^2}{4\eta kT}\frac{R^4}{l}. \tag{B.4}$$

Using the values given above for the dimensions of the capillary, the pressure p_0, temperature T, the source intensity can be estimated to be $I(0) = 8.4 \times 10^{18}$ He $\mathrm{s}^{-1}\mathrm{sr}^{-1}$.

Appendix C

Influence of collisions

C.1 Signal decrease by collisions

The two cross wire scanners are 1.95 m apart. In this region the atomic beam parameters (FWHM, flux) can be influenced by collisions between atoms in the atomic beam or collisions between atoms from the atomic beam and atoms in the background gas. The effect of these collisions can be effectively described by an absorption of particles. The transmission T is described by Beer's law

$$T = exp\left(-\frac{g}{v}nQl\right), \tag{C.1}$$

in which l is the length of interaction, in this case taken to be 1.95 m, the distance between the two scanners, Q the cross section of collisions, estimated to be 100 $Å^2$, n the density of particles, v the velocity of an atom from the atomic beam and g the relative collision velocity. When collisions between particles with orthogonal trajectories are considered, g is given by $\sqrt{u^2+v^2}$, with u the velocity of the other atom.

If this atom is an atom from the thermal background gas, its velocity is higher than the velocity of the particles in the atomic beam, which are emitted from a liquid nitrogen cooled source. This scaled collision velocity is estimated to be $1.5v$ for collisions with the background gas.

C.2 Collisions between atoms in the collimated beam

This density can be estimated by considering the flux of particles ($\dot{N} = 15 \times 10^{10}$ s^{-1}) through the FWHM (about 10 mm) of the beam profile and assuming a velocity of 1300 m/s. This gives a density of $n = 1.2 \times 10^{12}$ m^{-3}. The number of collision between atoms in the collimated beam is negligible or this density.

C.3 Collisions with residual gas atoms

The vacuum system in concern consists of 3.4 m long tube of the Zeeman slower with a diameter of 80 mm. A flow resistance of 98 mm with a diameter of 8 mm connects the Zeeman slower with the collimator chamber. In the middle of the Zeeman slower, 1.5 m in front of the end of the tube, a turbo molecular pump with a pumping speed of 250 l/s for He is located. Above this turbo pump the first wire scanner is located. A tube of 0.35 m long with a diameter of 25 mm connects the Zeeman slower tube with the compressor chamber. This chamber is also pumped on with a turbo molecular pump with a pumping speed of 250 l/s. Above this turbo pump, the second wire scanner is located.

At every point between the two vacuum pumps the influence of the two vacuum pumps can be calculated using the conductance of the tubes connecting the point to both vacuum pumps. This way the pumping speed at every point between the two vacuum pumps can be calculated. The average pumping speed in this area is calculated to be 115 l/s.

The pressure is measured above the first vacuum pump with a penning ionization pressure gauge. The sensitivity of this pressure gauge for He with respect to the sensitivity for N_2 is 0.16. When no helium gas is let into the vacuum system the pressure is 1×10^{-8} mbar N_2 equivalent. Because the compression ratio of the turbo pump for He is relatively low, a substantial fraction of the residual gas will be helium. When the source is operational, the pressure measured with this gauge is about 2×10^{-7} mbar N_2 equivalent. Using the ideal gas law, the local particle density can be calculated. This density is $n = 3 \times 10^{16}$ He m^{-3}.

The effective density between the two turbo pumps, i.e. between the two wire scanners, is the density above the first turbo pump, scaled with the ratio between the maximum and the effective pump speed. Using equation (C.1) the transmittance of this gas now can be calculated. The transmittance is calculated to be 83%.

Appendix D

Measuring the beam profile through a circular aperture

Consider a Gaussian distributed beam profile with a FWHM σ

$$P(x,y) = \mathcal{C}e^{-4\ln 2x^2/\sigma^2}e^{-4\ln 2y^2/\sigma^2}. \tag{D.1}$$

Integrating over one dimension gives the profile measured with a wire scanner, $P(x)$ is given by

$$P(x) = \int_{-\infty}^{\infty} \mathrm{d}y P(x,y) = \mathcal{C}\sqrt{\frac{\pi\sigma^2}{4\ln 2}}e^{-4\ln 2x^2/\sigma^2}. \tag{D.2}$$

The flux which is now within the FWHM is $0.862\mathcal{C}\sigma^2$.

When a circular aperture with radius R is shielding the wire scanner from the atomic beam, the measured signal $P'(x)$ can be calculated by

$$P'(x) = \int_{-\sqrt{R^2-x^2}}^{\sqrt{R^2-x^2}} \mathrm{d}y P(x,y). \tag{D.3}$$

The solution of this integral is

$$P'(x) = \mathcal{C}\sqrt{\frac{\pi\sigma^2}{4\ln 2}}\mathrm{erf}\sqrt{4\ln 2\frac{R^2-x^2}{\sigma^2}}e^{-4\ln 2x^2/\sigma^2}. \tag{D.4}$$

When the radius of the aperture R is equal to the FWHM of the beam profile σ, the measured FWHM follows from solving $\frac{P'(X)}{P'(0)} = \frac{1}{2}$. This equation holds for $X = 0.492\sigma$. The measured FWHM is $2X$, is 2% smaller than the real FWHM. The flux within the measured FWHM is $0.833\mathcal{C}\sigma^2$. This value is 4% lower than with no aperture present.

Appendix E

DBR diodelaser

The lasers used in our experiment are Distributed Bragg Reflection disdelasers (SDL 6702-H1). For each laser cooling element a diodelaser is used. For the cavity some power of the laser for the lens or for the compressor is taken. The lasers are specified for 50 mW output power, but all at different operating currents. The spectral linewidth of the lasers is specified to be 3 MHz. In table E.1 an overview is given of some characteristics of the diodelasers.

The output power is less than 50 mW because the current through the laser is kept lower than the specified operating current and because there is a small collimation lens with N.A.=0.55, placed in front of the laser, which clips of some laser power.

The power source of this laser is a home made diode laser control box, see [BRU89]. With this control box the current through the laser and the temperature of the laser can be adjusted.

The temperature of the laser is stabilized by measuring the temperature with the internal NTC resistance, comparing this value with the required value and adjusting the heating with the internal Peltier element. The temperature can be kept constant up to 1 mK. Increasing the temperature decreases the wavelength of the laser.

The current through the laser can be adjusted from 0 mA up to 200 mA, with an accuracy of 1 μA. Adjusting the current can be done by hand or with a computer. When above threshold, both the wavelength of the laser and the power of the laser are linear with the current through the laser. The temperatures are set such that the working frequency of the laser is at almost the maximum current through the laser.

diode for	maximum current (mA)	working current (mA)	output power (mW)	$d\omega/dI$ ((2π) MHz/mA)
collimator	180	173	49	$(117 \pm 1) \times 10$
Zeeman slower	200	175	31	722
absorption spectroscopy	170	??	??	490

Table E.1: Some characteristic of the laserdiodes.

The dependance of the frequency of the laser on the current through the laser is for every laser determined with a different method. For the laser for the collimator and the lens this number is determined by comparing the difference in current between the $^3P_1$ and the $^3P_2$ peak in the saturated absorption spectrum, with the very accurately known frequency difference between these transitions. This is discussed in section 2.4.1. For the laser for the Zeeman slower this number is determined by comparing the difference in the beat frequency with the collimator laser, with the variation in current.

Appendix F

Detectors

The light sensitive element in all used detectors is an InGaAs photodiode. It has a sensitivity of 0.8 μW/μA for λ=1083 nm. Its effective area has a diameter of 80 μm. With a 5 V bias voltage the bandwidth of the photodiode is 1.5 GHz. The operational amplifiers used in the detectors are the types OPA604 and LP27.

F.1 Normal detector

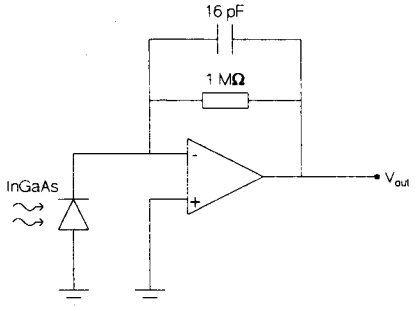

This detector is used in the saturated absorption spectroscopy setups. The current from the photodiode is amplified over the resistance and the capacitor. The combination of these serve as a low pass filter with a cut-off frequency of 10 kHz, much higher than the 1025 Hz modulation frequency used. Its gain is therefore only determined by the resistance of 1 MΩ, which means that the detectors sensitivity is 1 V/μA.

F.2 High frequency detector

This detector consists of a photodiode with 5 V negative bias to increase the photodiodes sensitivity. The signal is measured over a resistance of 47 Ω. The signal measured with this detector is amplified with a pulse preamplifier (Phillips Scientific, model 6954) which

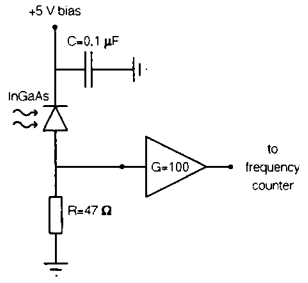

can amplify signals with a frequency up to 1.7 GHz and has a voltage gain of 100. This detector is used to perform the hetrodyne mixing signal which has a frequency of about 750 MHz.

The value of the resistance is chosen to match the output impedance of the detector with the input impedance of the amplifier used, which is 50 Ω. Because also the output of the amplifier has an impedance of 50 Ω, the input impedance of the apparatus which measures the amplifiers signal should also be 50 Ω.

F.3 AC-coupled detector

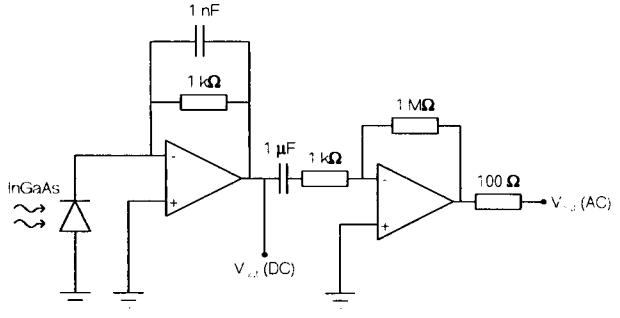

This detector is used for the absorption-velocity measurement setup. Because the information of interest is the AC signal which is on a large DC background an AC coupled detector is used. The first part of the amplifier, between the photodiode and the DC output, is similar to the amplifier discussed in F.1. Its cut off frequency is 160 kHz, much higher than the 1025 Hz modulation frequency. The transimpedance gain of the DC amplifier is 1 mV/μA.

The second part is a AC amplifier. The combination of the condensator of 1 μF and the resistance of 1 kΩ define a high-pass filter with a cut off frequency of 160 Hz, lower than the 1025 Hz used. The resistances of 1 MΩ and 1 kΩ define an amplification factor of 1000. The gain of the AC amplifier is 1 V/μA for frequencies of 1 kHz. The resistance of 100 Ω is inserted to match the impedance to the input impedance of the device that measures the amplified signal.

Appendix G

Uniform slowing

The position dependence of the velocity of a uniformly slowed particle can be derived from Newton's equations

$$\begin{aligned} z(t) &= z(0) + v(0)t + \frac{1}{2}at^2, \\ v(t) &= v(0) + at, \\ a(t) &= a. \end{aligned}$$

with $z(t)$, $v(t)$ and $a(t)$ the position, velocity and acceleration of a particle at a certain time t, $z(0)$ and $v(0)$ are the initial conditions, and a the constant acceleration. The relation between the velocity at a certain time t and the position at this time is given by

$$v(t)^2 - v(0)^2 = 2a(z(t) - z(0)). \tag{G.1}$$

When the position and velocity at a time τ are known, also the acceleration can be calculated

$$a = \frac{v(\tau)^2 - v(0)^2}{2(z(\tau) - z(0))}. \tag{G.2}$$

If z(0)=0 and τ is the time on which the velocity reaches zero, $v(\tau) = 0$ the position dependance of the velocity is given by

$$v(t) = v(0)\sqrt{1 - \frac{z(t)}{z(\tau)}}, \tag{G.3}$$

with $z(\tau)$ the positon on which the velocity has reached zero.

Appendix H

Heterodyne mixing

When two light fields with frequencies ω_1 and ω_2 and a phase difference of δ spatially overlap on a detector a beat signal can be measured. The electric field on the detector is

$$E = E_1 \cos(\omega_1 t) + E_2 \cos(\omega_2 t + \delta).$$

If $E_1 > E_2$ this can be written as

$$E = (E_1 - E_2)\cos(\omega_1 t) + E_2 \left\{\cos\omega_1 t + \cos(\omega_2 t + \delta)\right\}.$$

This gives rise to an intensity I of

$$\begin{aligned}
I &\sim \left\{E_1 \cos(\omega_1 t) + E_2 \cos(\omega_2 t + \delta)\right\}^2 \\
&= (E_1 - E_2)^2 \cos^2\omega_1 t + E_2(E_1 - E_2)\cos\omega_1 t \left\{\cos\omega_1 t + \cos(\omega_2 t + \delta)\right\} \\
&\quad + E_2^2 \left\{\cos\omega_1 t + \cos(\omega_2 t + \delta)\right\}^2 \\
&= (E_1 - E_2)^2 \cos^2\omega_1 t + E_2(E_1 - E_2)\left\{\cos\left(\frac{3\omega_1 + \omega_2}{2}t + \frac{\delta}{2}\right) + \cos\left(\frac{\omega_1 + \omega_2}{2}t + \frac{\delta}{2}\right)\right\} \\
&\quad + E_2^2 \left\{1 + \cos\left[(\omega_1 + \omega_2)t + \delta\right] + \left\{1 + \cos\left[(\omega_1 + \omega_2)t + \delta\right]\right\}\cos\left[(\omega_1 - \omega_2)t - \delta\right]\right\}.
\end{aligned}$$

Measuring the intensity with a detector that can measure the frequency difference between the two signals means averaging the intensity over time periods longer than $\frac{2\pi}{\omega_1}$ or $\frac{2\pi}{\omega_2}$, but shorter than $\frac{2\pi}{|\omega_1 - \omega_2|}$. This gives:

$$\begin{aligned}
I &\sim \frac{(E_1 - E_2)^2}{2} + 0 + E_2^2 \left\{1 + 0 + \cos\left[(\omega_1 - \omega_2)t - \delta\right] + 0\right\} \\
&= \frac{(E_1 - E_2)^2}{2} + E_2^2 + E_2^2 \cos\left[(\omega_1 - \omega_2)t - \delta\right].
\end{aligned}$$

From this it is clear that the only frequency that can be measured is the frequency difference of the two light fields.

Appendix I

Technology assessment

Although lasercooling is a relatively young and fundamental field of research, it is a technique with much potential. Not only is it possible to increase the intensity of atomic beams by adding a simple instrument like a collimator, it is also possible to manipulate the atomic beam in several other ways. There are the manipulations briefly described in this thesis, e.g. focusing of the atomic beam, or compressing the beam into a beam of small diameter. These manipulations are performed by creating a creating a force which is increasing for larger distances from the beam axis. This spatially varying force is achieved by using quadrupole magnetic fields and using resonant interaction of the atoms with the laser.

At the moment a technique is being studied in which the nodes of a standing light field are used as lenses to focus iron atoms in an atomic beam. The wavelength of the used laser light is several linewidths detuned from the lasercooling transition of the iron atom. This way nanometer scale areas of iron can be deposited. By moving the sample, many identical nanoscale structures of iron can be deposited at the same time using a single beam of iron atoms.

On a more fundamental scale, the investigation of of quantum light fields and the interaction of these light fields with atoms may produce information, which can be used in future applications. In particular quantum computation must be mentioned as such a future application.

In this technique the quantum state of the light field in the cavity is considered as information called a Q-bit. When more of these light fields are available calculations can be performed by combining the information in these light fields. The light field can be in a coherent superposition of states. The calculations can be performed on all states in this coherent superposition. This and the fact that the computations are on a quantum scale offer the possibility of extremely fast computation techniques.